DESIGN AND TESTING OF THE NAVIGATION MODEL FOR THREE AXIS STABILIZED EARTH ORIENTED SATELLITES APPLIED TO THE ATS-6 SATELLITE IMAGE DATA BASE

SSEC No.77.05.K1

A REPORT

from the space science and engineering center
the university of wisconsin-madison
madison, wisconsin

Permanent file

DESIGN AND TESTING OF THE NAVIGATION MODEL FOR THREE AXIS STABILIZED EARTH ORIENTED SATELLITES APPLIED TO THE ATS-6 SATELLITE IMAGE DATA BASE

Progress Report for Period Ending 31 October 1977

Contract Number NAS5-20974

For

National Aeronautics and Space Administration
Goddard Space Flight Center
Greenbelt, Maryland 20771

By

W. W. Kuhlow
G. C. Chatters

University of Wisconsin
Space Science and Engineering Center
1225 West Dayton Street
Madison, Wisconsin 53706

May 1977

TABLE OF CONTENTS

LIST OF FIGURES

LIST OF TABLES

I. INTRODUCTION

This report summarizes the work done thus far under Contract NAS5-20974 concerning development of the three-axis stabilized navigation model for purpose of measuring winds from the ATS-6 image data.

Over the past year our work with the ATS-6 attitude telemetry data and the associated image data has shown that the telemetry data is not of sufficient quality for the purposes of measuring winds accurate to a few meters per second. However, a methodology has been developed to account for the relative attitude changes between successive ATS-6 images which allows reasonable high-quality wind sets to be produced. The method consists of measuring the displacements of the right and left infrared earth edges between successive ATS-6 images as a function of scan line; from these measurements the attitude changes can be deduced and used to correct the apparent cloud-displacement measurements. The preprocessing time and effort for obtaining these earth-edge measurements is comparable to that of obtaining landmark measurements.

The wind data sets generated from ATS-6 using the "earth-edge" methodology mentioned above were compared with those derived from the SMS-1 images (and model) covering the same time period. Quantitative comparisons for low-level trade cumuli were made at interpolated uniformly spaced grid points and for selected individual comparison clouds. There were sixteen grid points at which vector comparisons could be made between the ATS-6 and SMS-1 derived winds. The differences between each satellite-derived wind vector component at each of these points were all less than 2 meters per second with a root-mean-square difference of less than 1 meter per second for both vector components. Wind direction differences did not exceed 13°. For the nine

selected individual comparison clouds, the root-mean-square differences for the U and V components were 1.0 and 1.2 meters per second with a maximum wind direction difference of 15°.

The major task remaining under this contract is the implementation of the ATS-6 model (including the new earth-edge methodology) to AOIPS system at GODDARD; this work is currently in progress.

II. ATS-6/SMS-1 CLOUD VELOCITY COMPARISON MEASUREMENTS

This section discusses the ATS-6 wind sets produced using the methodology discussed briefly in the INTRODUCTION and in more detail in SEC. III and compares them to the SMS-1 derived winds.

The background on the study area and the procedure used to obtain both ATS-6 and SMS-1 wind sets using McIDAS are given in the 31 June, 1976, NAS5-20974 progress report. The SMS-1 wind sets and all associated figures and measurements discussed in that report are reproduced here unchanged except for figure and table captions.

FIGURES II.1. and II.2. show the ATS-6 and SMS-1 low-level trade cumuli wind fields and FIGURES II.3. and II.4. their associated wind fields interpolated to .2° latitude/longitude grid points. TABLE II.1. summarizes the low-level wind-vector comparisons for small clouds which could be identified on both the SMS-1 and ATS-6 images, and TABLE II.2. summarizes the low-level wind-vector comparisons for the interpolated grid-point values shown in FIGS. II.3. and II.4. Note that the root-mean-square values in the component differences (ΔU_{rms}, ΔV_{rms}) are all about 1 m/sec for both the small comparison clouds and the interpolated grid-point values. The slight bias of the ATS-6 V-components to values smaller than the corresponding SMS-1 values for the small-cloud comparisons (TABLE II.2.) is curious because these same clouds are scattered throughout the clouds in the study area from which the interpolated grid-values are obtained -- and the interpolated ATS-6 V-component values are slightly higher on the average than their SMS counterparts. This small-cloud bias most likely results from the small number of clouds measured.

FIGURES II.5. and II.6. are plots of the high-level ATS-6 and SMS-1

winds. Quantitative comparisons were not made because of the small number of measurements available.

FIGURE II.7. is a plot of the wind-vector differences of the successive pairs of ATS-6 images and serves as a quality check on the vectors. These vectors are related directly to those given in FIGURE II.1., where in this figure, the U-component, for example, was obtained by averaging U_{12} and U_{23} where U_{12} is the U-component measured for a cloud between images T_1 (164223Z) and T_2 (170658Z) and U_{23} between images T_2 and T_3 (173134Z). In FIG. II.7. however, the U-component is $(U_{12} - U_{23})/2$ and therefore is a measure of the distance from the mean of these two values. The same discussion applies to the V-component. Thus, FIG. II.7. is an indication of the consistency and accuracy of the ATS-6 wind-measuring process. Ideally these vector differences would be zero for non-accelerating clouds (effectively true for this study area), and if not zero, at least small and pointing in random directions. This latter condition is generally satisfied as implied by FIG. II.7. TABLE II.3. presents the vector differences for the two ATS-6 image pairs for the same small-cloud measurements given in TABLE II.1. and also makes comparisons to the SMS-1 values. The standard deviations given in TABLE III.3. show that there is slightly less variation between the ATS-6 wind-vector component measurements $U_{12}(V_{12})$ and $U_{23}(V_{23})$ than there is between $U_{12}(V_{12})$ and the corresponding averaged SMS components $U_A(V_A)$. Furthermore, the averages of the ATS-6 vector-component differences are less than 0.5 m/sec.

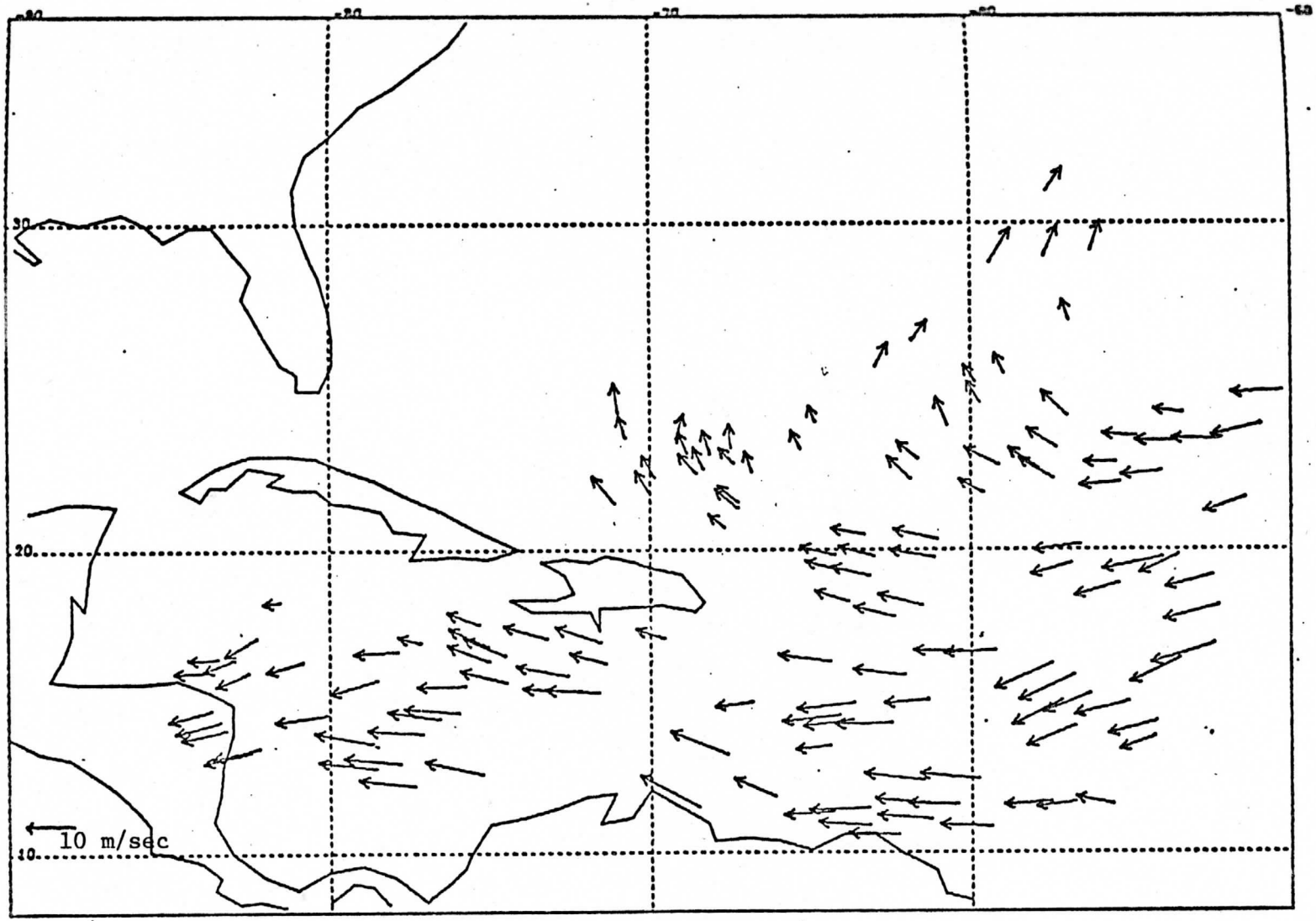

FIGURE II.1. LOW-LEVEL WINDS FROM ATS-6 computed by using earth-edge displacement measurements to account for attitude changes. Length of vectors are proportional to velocity. Reference vector shown in lower left-hand corner.

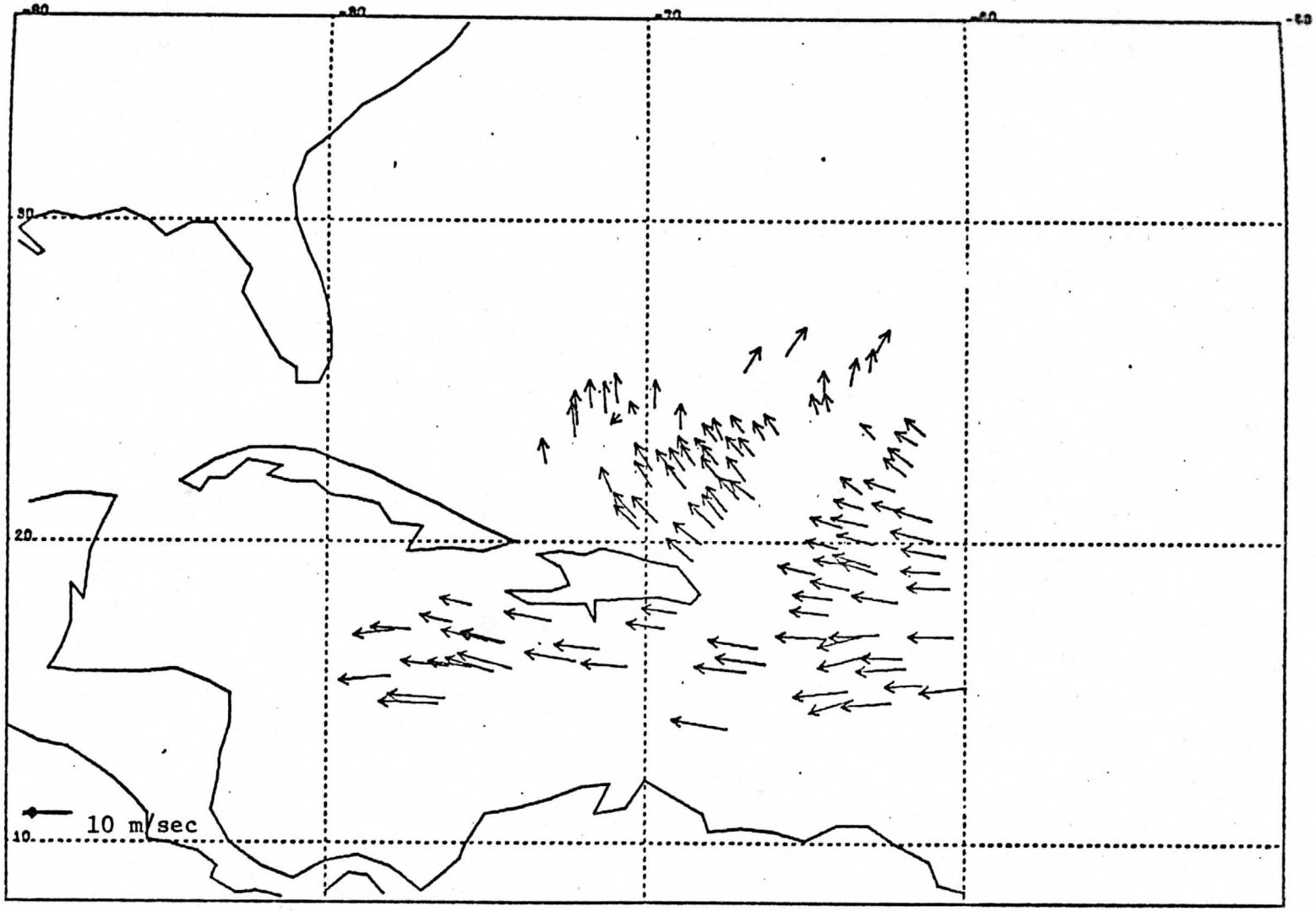

FIGURE II.2. LOW-LEVEL WINDS FROM SMS-1 covering same time period as ATS-6 wind field shown in FIG. II.1. SMS-1 wind field is of smaller geographical extent than than of ATS-6 due to the former satellite's higher resolution. Reference vector is shown in lower left-hand corner.

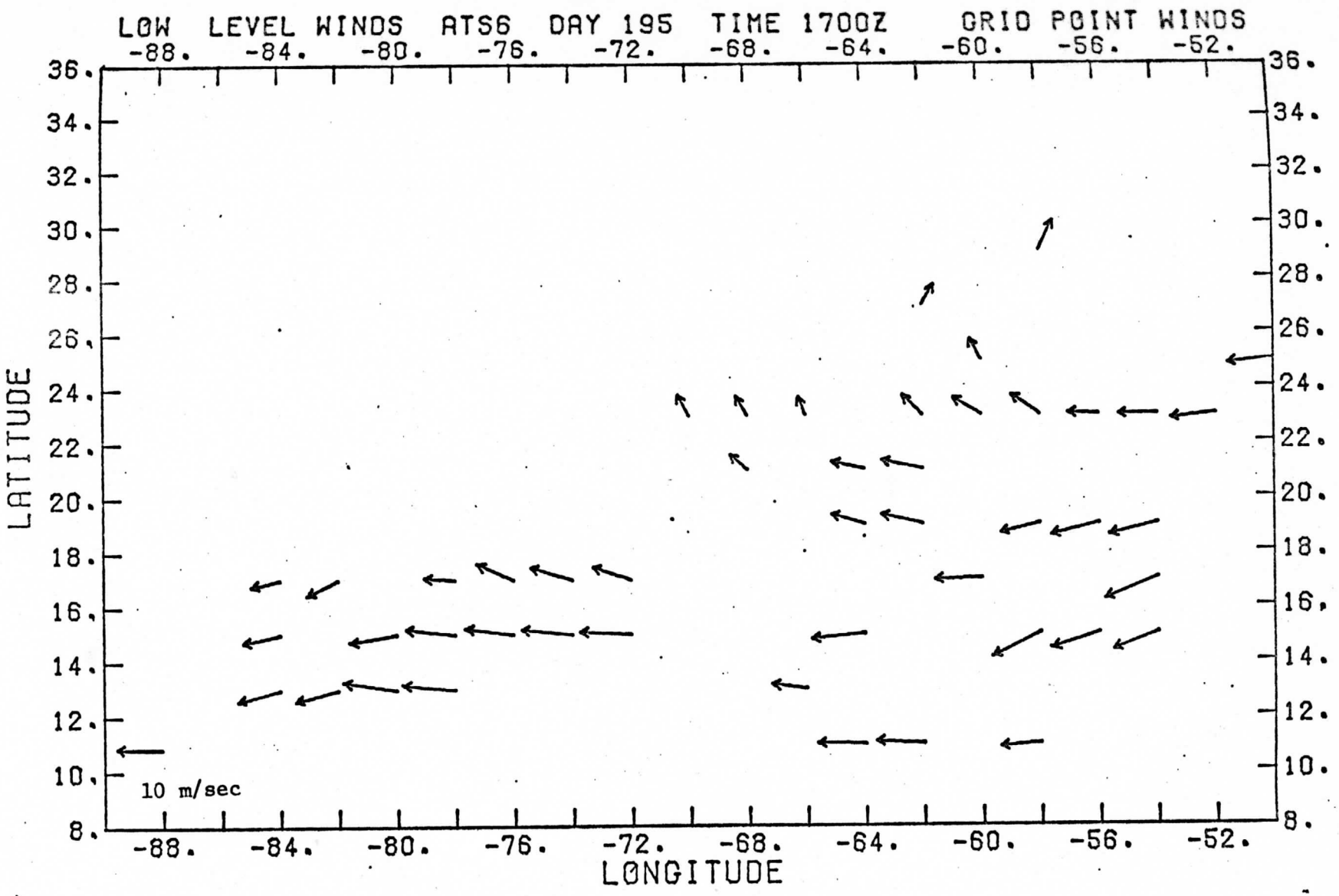

FIGURE II.3. LOW-LEVEL ATS-6 WINDS INTERPOLATED AT 2° GRID POINTS from the data shown in FIG. II.1. Vector components at each grid point for which both ATS-6 and SMS-1 (FIG. II.4) non-zero vectors are available are tabulated and compared in TABLE II.2. Reference vector is shown in lower left-hand corner.

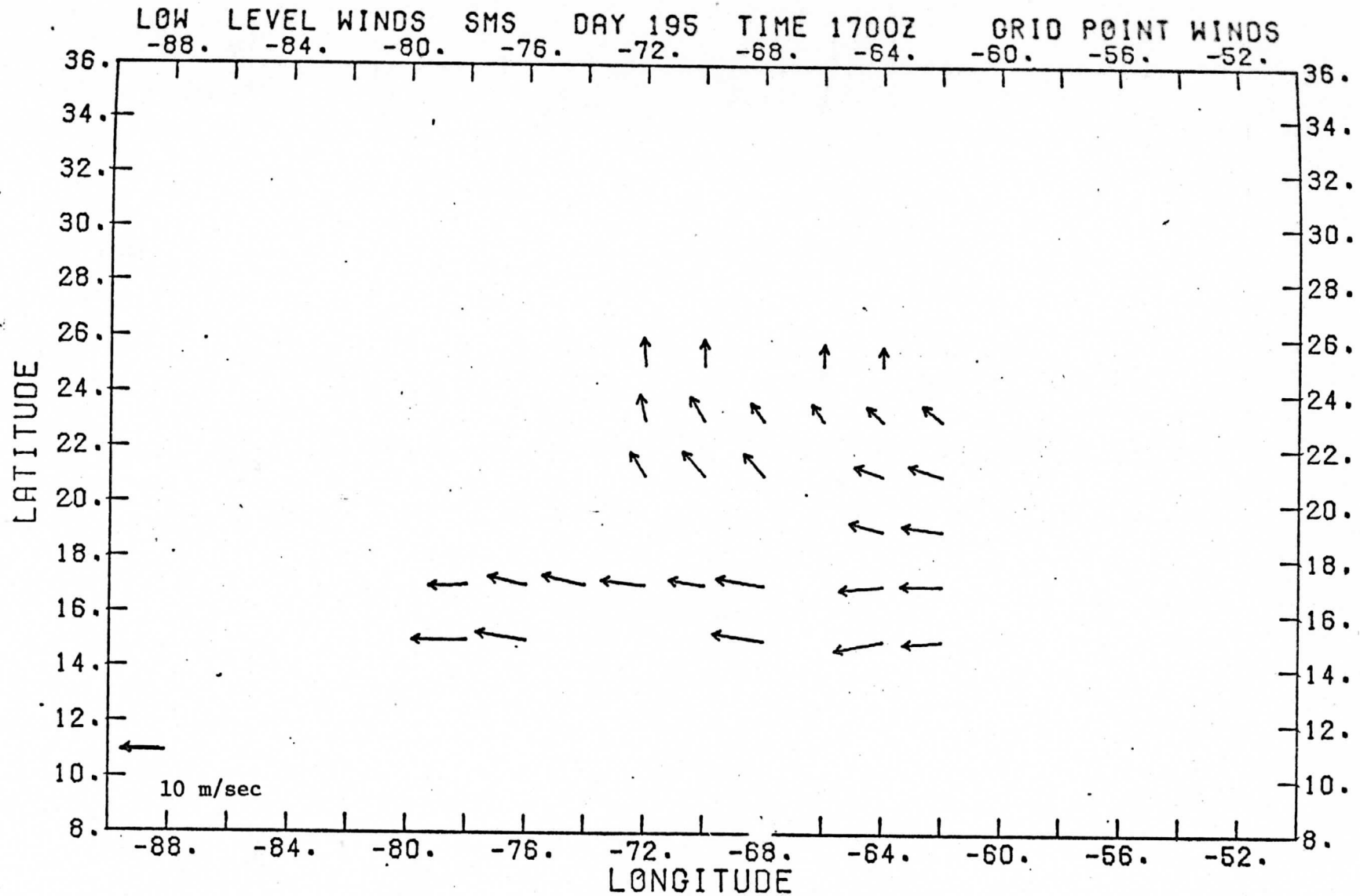

FIGURE II.4. LOW-LEVEL SMS-1 WINDS INTERPOLATED AT 2° GRID POINTS from data shown in FIG. II.2. Reference vector is shown in lower left-hand corner.

No.	SMS		SMS		ATS-6		DIFFERENCE			
	LAT	LON	U(m/s)	V(m/s)	U(m/s)	V(m/s)	ΔU	ΔV	$\lvert\vec{V}_A-\vec{V}_S\rvert$	$\Delta\phi$
1	22.99	-66.75	- 2.82	4.25	- 1.37	4.14	1.45	-0.11	1.45	15°
2	21.75	-67.48	- 4.14	5.27	- 4.42	3.94	-0.28	-1.33	1.36	-10°
3	21.12	-67.76	- 3.99	5.15	- 3.28	2.61	0.71	-2.54	2.64	-14°
4	20.10	-63.46	- 7.45	2.51	- 7.65	1.98	-0.20	-0.53	0.57	- 4°
5	18.21	-62.81	- 9.14	2.31	- 7.87	2.16	1.27	-0.15	1.28	1°
6	16.10	-74.88	-10.95	3.76	- 9.48	2.64	1.47	-1.12	1.85	- 3°
7	16.05	-67.13	-11.22	1.36	-11.08	0.15	0.14	-1.21	1.22	- 6°
8	15.97	-63.84	-11.00	-2.28	-12.25	-3.76	-1.25	-1.48	1.94	- 5°
9	15.17	-64.34	-11.16	-1.44	-11.79	-1.47	-0.63	-0.03	0.63	0°
							$\overline{\Delta U}$=0.30	$\overline{\Delta V}$=-0.94		
							S(ΔU)=0.98	S(ΔV)= 0.82		
							ΔU_{rms}=0.97	ΔV_{rms}= 1.22		

TABLE II.1. ATS-6/SMS-1 LOW-LEVEL WIND-VECTOR COMPARISONS FOR SMALL CLOUDS which could be identified on both the SMS-1 and ATS-6 images. The averages $\overline{X}$ and standard deviations S (both in m/s) are given for the U- and V-component differences between the two sets of wind vectors; $\lvert\vec{V}_A-\vec{V}_S\rvert$ is the magnitude of their vector differences and $\Delta\phi$ the differences in wind direction.

		SMS-1		ATS-6		DIFFERENCE			
LAT	LON	U (m/s)	V (m/s)	U (m/s)	V (m/s)	ΔU	ΔV	$\lvert V_A - V_S \rvert$	Δφ
23	-70	- 3.09	5.18	- 2.31	4.37	.78	- .81	1.12	3°
23	-68	- 2.67	3.89	- 2.28	3.96	.39	.07	.40	5°
23	-66	- 2.46	3.72	- 1.59	3.79	.87	.07	.87	11°
23	-62	- 4.30	3.24	- 4.26	3.98	.04	.74	.74	6°
21	-68	- 4.16	5.00	- 3.65	3.15	.51	-1.85	1.92	- 9°
21	-64	- 5.93	2.13	- 7.03	1.61	-1.10	- .52	1.22	- 7°
21	-62	- 7.14	2.22	- 8.88	1.85	-1.74	- .37	1.78	- 6°
19	-64	- 7.21	1.83	- 7.21	2.06	.00	.23	.23	2°
19	-62	- 8.56	1.15	- 9.05	2.05	- .49	.90	1.02	5°
17	-78	- 8.03	- .25	- 6.71	0.37	1.32	.62	1.46	5°
17	-76	- 8.06	1.79	- 7.80	3.44	.26	1.65	1.67	11°
17	-74	- 9.15	2.08	- 9.03	2.69	.12	.61	.62	4°
17	-72	- 9.24	1.08	- 8.27	2.75	.97	1.67	1.93	12°
15	-78	-11.60	- .06	-10.81	1.15	.79	1.21	1.45	6°
15	-76	-10.49	1.70	-10.47	1.31	.02	- .39	.39	- 2°
15	-64	-10.13	-1.99	-11.61	-1.13	-1.48	.86	1.71	6°
						$\overline{\Delta U}$=0.09	$\overline{\Delta V}$=0.29		
						S(ΔU)=0.88	S(ΔV)=0.94		
						ΔU_{rms}=0.86	ΔV_{rms}=0.95		

TABLE II.2. ATS-6/SMS-1 LOW-LEVEL WIND-VECTOR COMPARISONS FOR INTERPOLATED GRID-POINT VALUES. Vector components at each grid point for which both ATS-6 (FIG. II.3.) and SMS-1 (FIG. II.4.) non-zero vectors are available are given. The averages $\overline{X}$ and standard deviations S (both in m/s) are given for the U- and V-component differences.

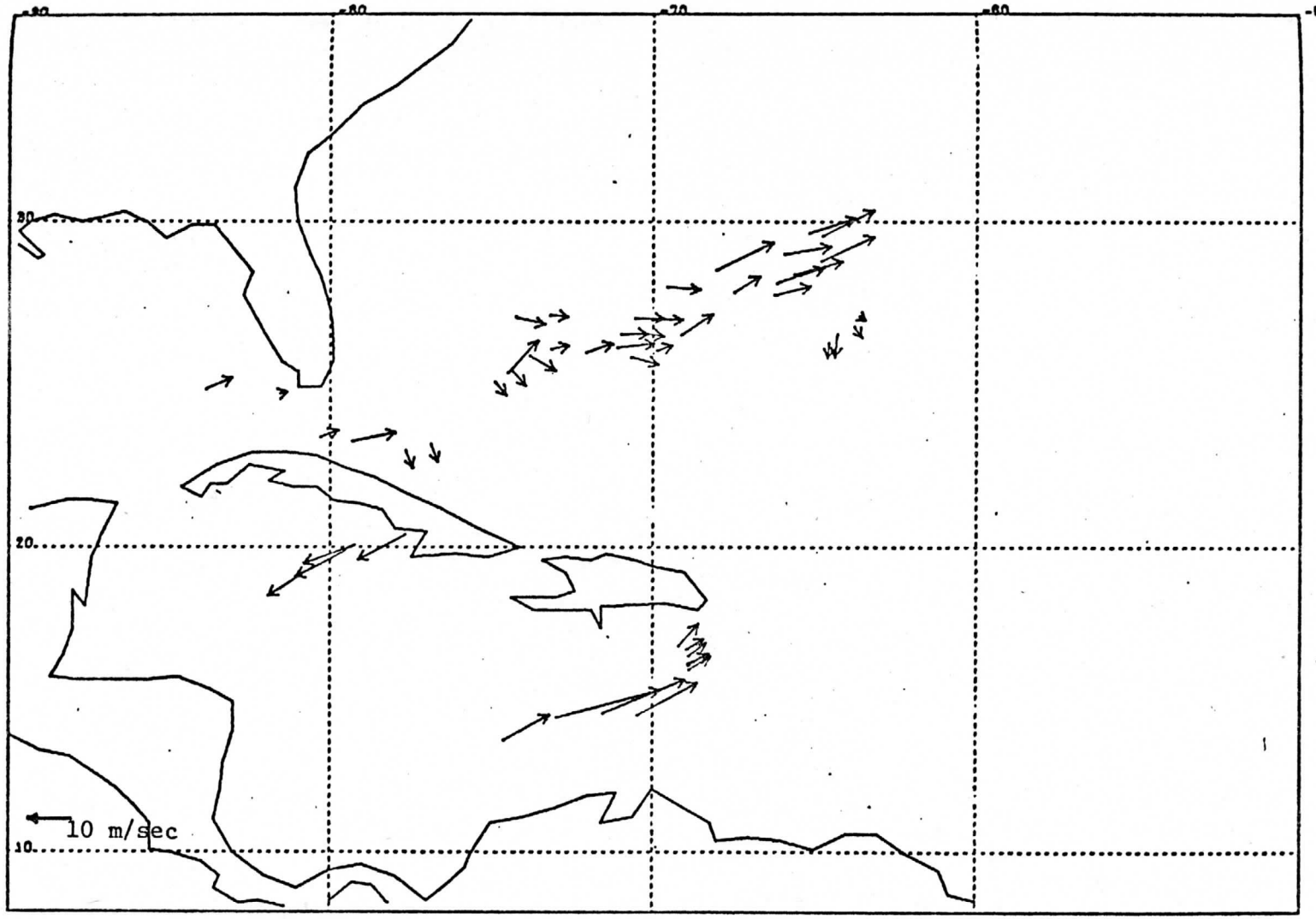

FIGURE II.5. HIGH-LEVEL ATS-6 WINDS derived from same imagery as ATS-6 low-level winds.

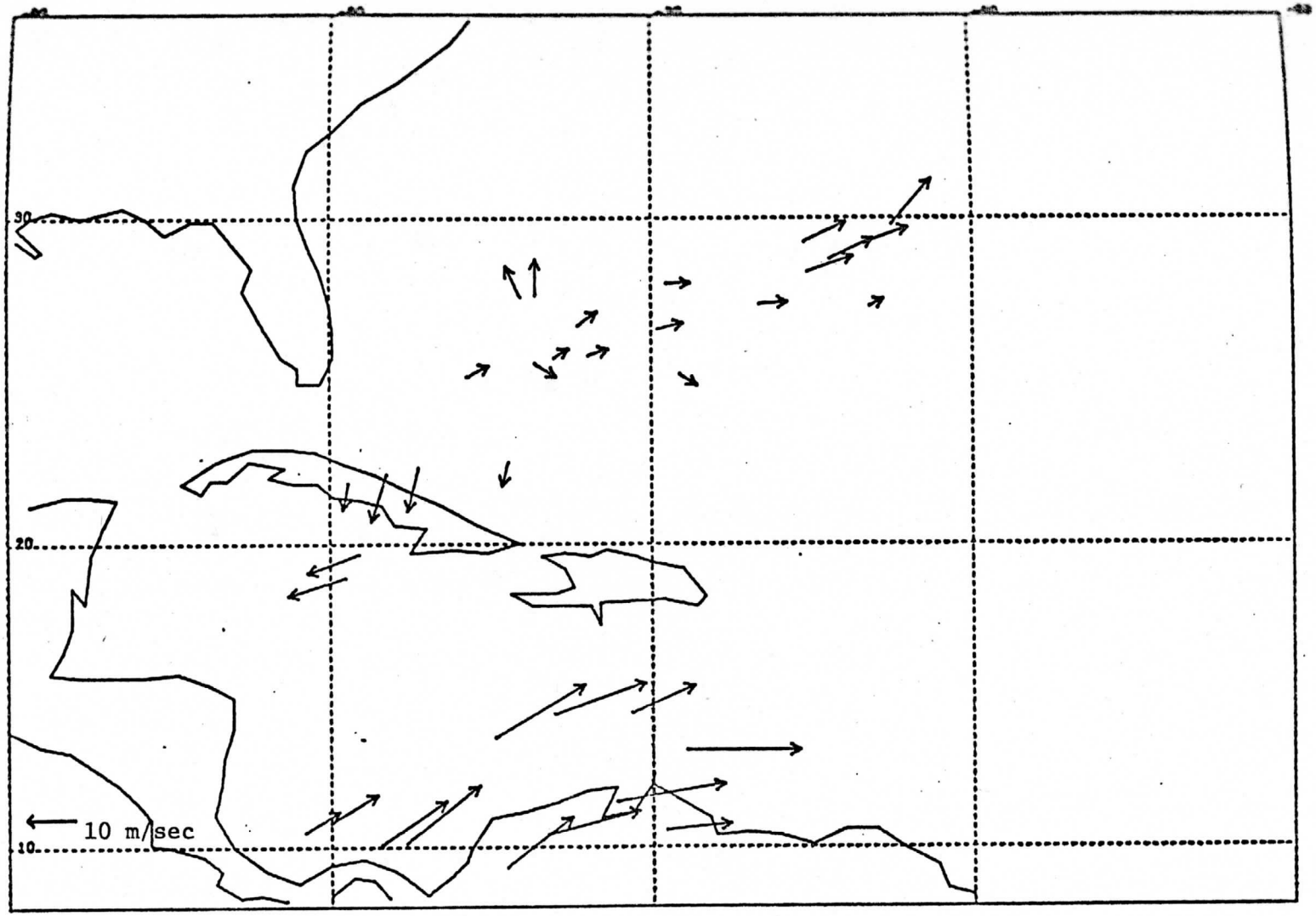

FIGURE II.6. HIGH-LEVEL SMS-1 WINDS derived from same imagery as SMS-1 low-level winds.

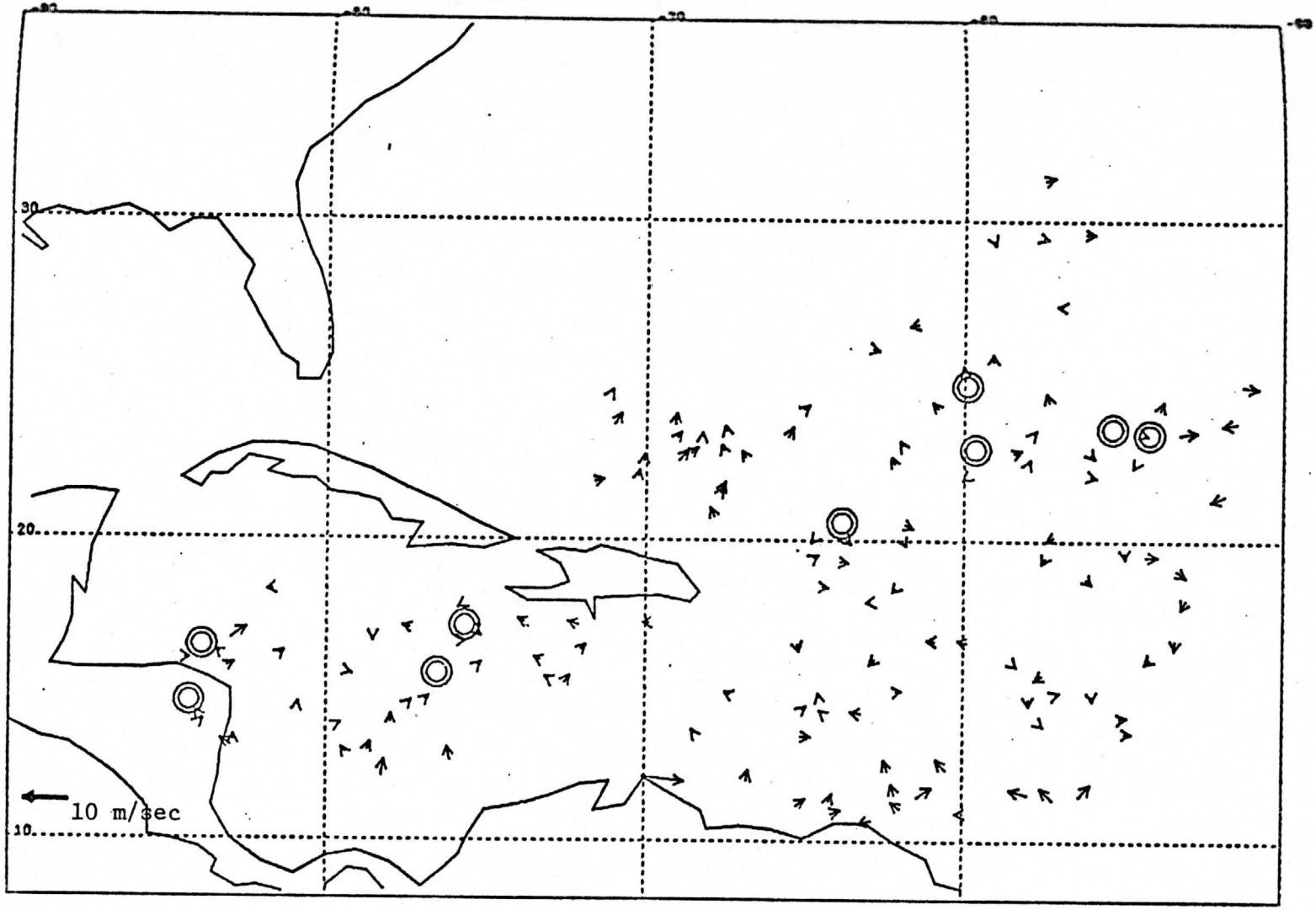

DAY 74195 TIME170658 900-900 MB WINDS

FIGURE II.7. ATS-6 WIND-VECTOR DIFFERENCES. Vector components are $(U_{12} - U_{23})/2$ and $(V_{12} - V_{23})/2$ where U_{ij}, V_{ij} are the velocity components measured from the ith - jth image pair. These values are tabulated in TABLE II.3. and compared to SMS-1 values. Double circles in figure indicate vectors of zero magnitude.

No.	ATS-6			SMS		ATS-6			SMS	
	U_{12}(m/s)	U_{23}(m/s)	ΔU_A	U_S	ΔU_S	V_{12}(m/s)	V_{23}(m/s)	ΔV_A	V_S	ΔV_S
1	- 2.07	- 0.67	-0.70	- 2.82	0.75	5.29	3.00	1.15	4.25	1.04
2	- 3.84	- 5.00	0.58	- 4.14	0.30	4.85	3.04	0.91	5.27	-0.42
3	- 4.03	- 2.54	-0.75	- 3.99	-0.04	4.22	1.01	1.61	5.15	-0.93
4	- 6.71	- 8.60	0.95	- 7.45	0.74	1.51	2.45	-0.47	2.51	-1.00
5	- 8.16	- 7.60	-0.28	- 9.14	0.98	2.05	2.30	-0.13	2.31	-0.26
6	- 9.19	- 9.80	0.31	-10.95	1.76	3.06	2.24	0.41	3.76	-0.70
7	-12.51	- 9.66	-1.43	-11.22	-1.29	0.04	0.28	-0.12	1.36	-1.32
8	-12.52	-12.00	-0.26	-11.00	-1.52	-4.59	-2.95	-0.82	-2.28	-2.30
9	-11.13	-12.46	0.67	-11.16	0.03	-0.84	-2.11	0.64	-1.44	0.60
			$\bar{X}$=-0.10 S=0.79		$\bar{X}$=0.19 S=1.06			$\bar{X}$=0.35 S=0.80		$\bar{X}$=-0.59 S=1.00

TABLE II.3. WIND-VECTOR DIFFERENCES OF SUCCESSIVE PAIRS OF ATS-6 IMAGES and comparison to SMS-1 values. These data are for the same nine small clouds given in TABLE II.1. U_{12} is the U-component measured from ATS-6 images T_1 and T_2, U_{23} for images T_2 and T_3. $\Delta U_A = (U_{12} - U_{23})/2$ is the difference from their mean value and $\Delta U_S = U_{12} - U_S$ is the difference of U_{12} from the mean SMS-1 measured U-component U_S for the same cloud. The same definitions apply to the V-components. Averages $\bar{X}$ and standard deviations S given under the difference columns are in meters per second.

III. METHODOLOGY TO ACCOUNT FOR ATTITUDE CHANGES WHEN MEASURING AND COMPUTING WINDS

1. Method and Results

The method for removing the attitude changes between successive ATS-6 images by using earth-edge measurements is described below.

For simplicity let us assume that wind measurements are to be made between only two successively scanned ATS-6 images designated T_1 and T_2. The following procedure is followed:

(i) The two infrared images are loaded on successive TV frames on McIDAS with the same start-coordinates so chosen that the right earth-edges can be viewed and the scan lines cover the same scan-line range cooresponding to the study area. Using an image-matching technique, the displacement of the T_2-edge relative to the T_1-edge is measured along the scan lines in increments of approximately 10 TV-scan lines (5 ATS-6 scan lines) at a time until measurements have been made along the entire available earth edge. These data are recorded and curve fitted (see FIG. III.1.). It is important to point out that the image-matching technique used measures displacements only along scan lines and not perpendicular to it.

(ii) The same procedure as given in (i) is performed for the left earth edge corresponding to the same scan line range. These measurements result in data such as shown in FIG. III.2.

(iii) It is shown in Appendix A that from these right and left earth-edge displacement curves it is possible to compute the satellite displacements ($\Delta L(L)$, $\Delta E(L)$) of the T_2 - SSP (Sub-Satellite Point) relative to the T_1 - SSP as a function of mirror-scan line number L. (The resulting $\Delta L(L)$ curve and $\Delta E(L)$ curve derived from the curves presented in FIGS. III.1. and III.2. are shown in FIGS. III.3. and III.4. respectively). The ΔL curve is in effect

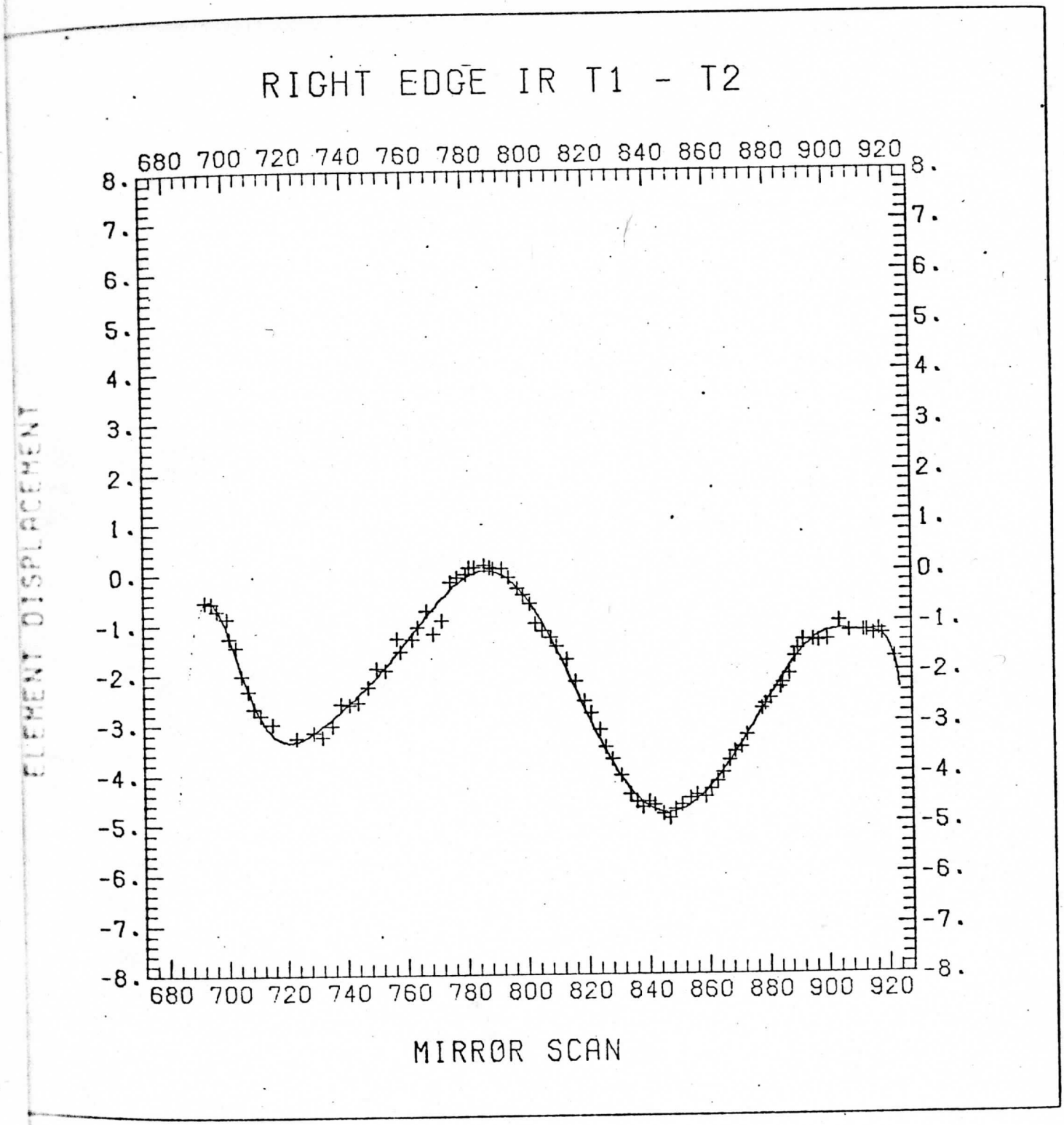

FIGURE III.1. RIGHT EARTH-EDGE DISPLACEMENT MEASUREMENTS as a function of mirror-scan number. The crosses show the actual measured displacements (measured by an image-matching technique) in resolution elements for a particular mirror-scan line of the T_2 image relative to the T_1 image of the right earth edge. The infrared digital imagery was used to obtain these measurements. The measured data were fit with a 15th degree polynomial curve shown in the figure.

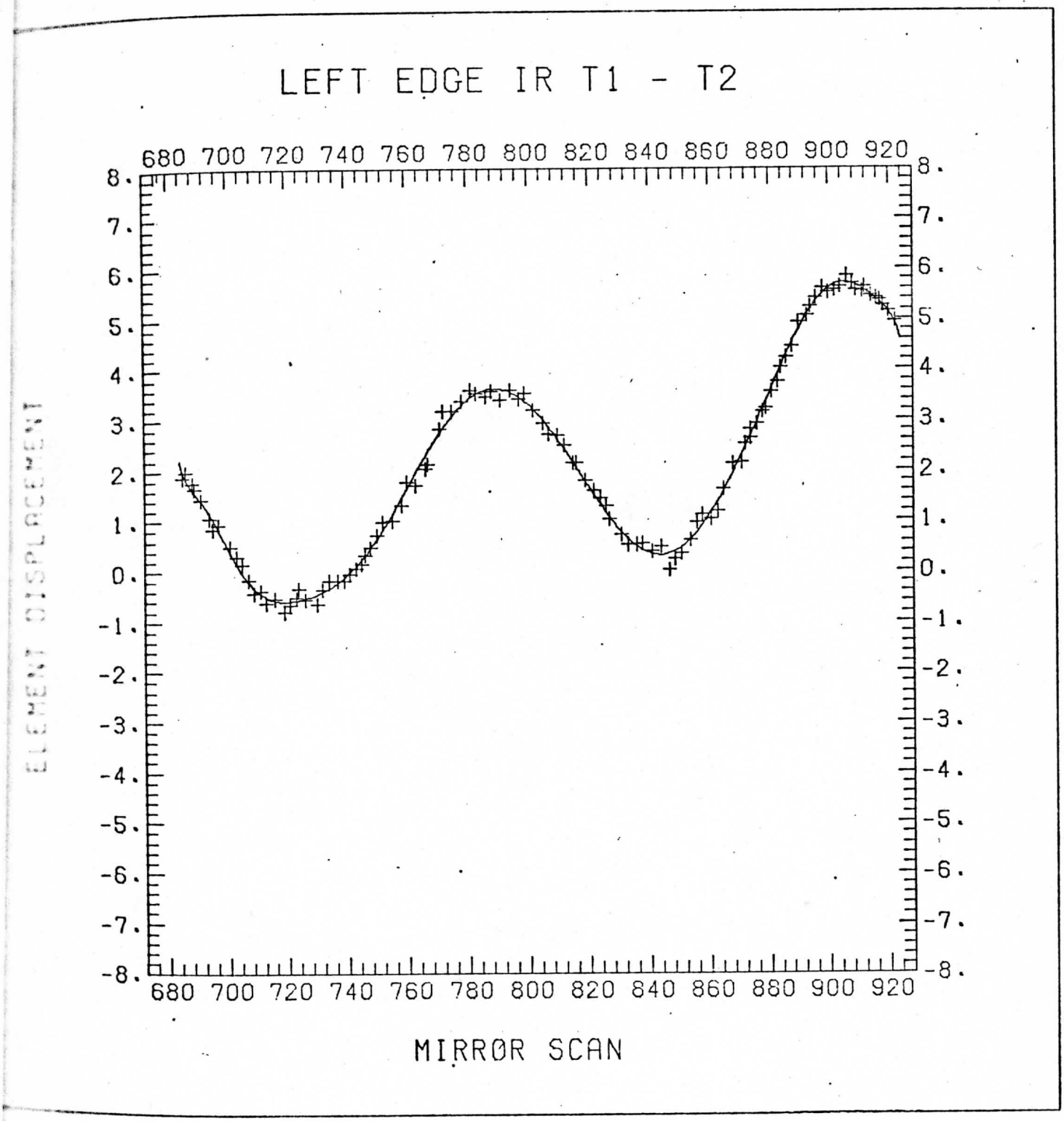

FIGURE III.2. LEFT EARTH-EDGE DISPLACEMENT MEASUREMENTS. These measurements are complementary to those shown in FIG. III.1.

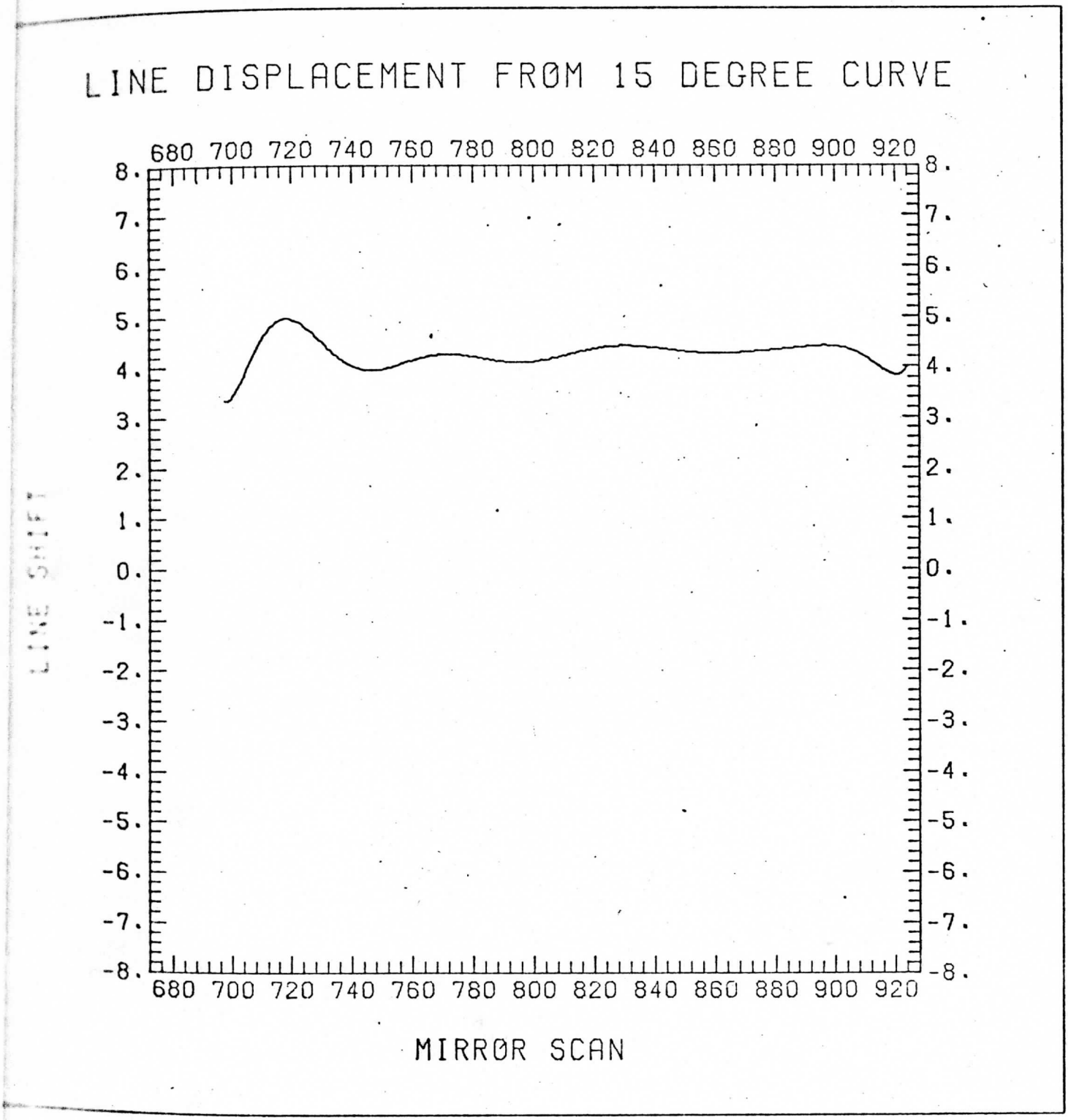

FIGURE III.3. RELATIVE LINE SHIFT OF THE T_2 SSP RELATIVE to the T_1-SSP as a function of mirror scan number. This curve was derived from the curves shown in FIGS. III.1. and III.2. by the methods discussed in the text and Appendix A. (SSP = Sub-Satellite Point; T_1 corresponds to ATS-6 image DAY 195 1974, 164223Z and T_2, 170658Z same day)

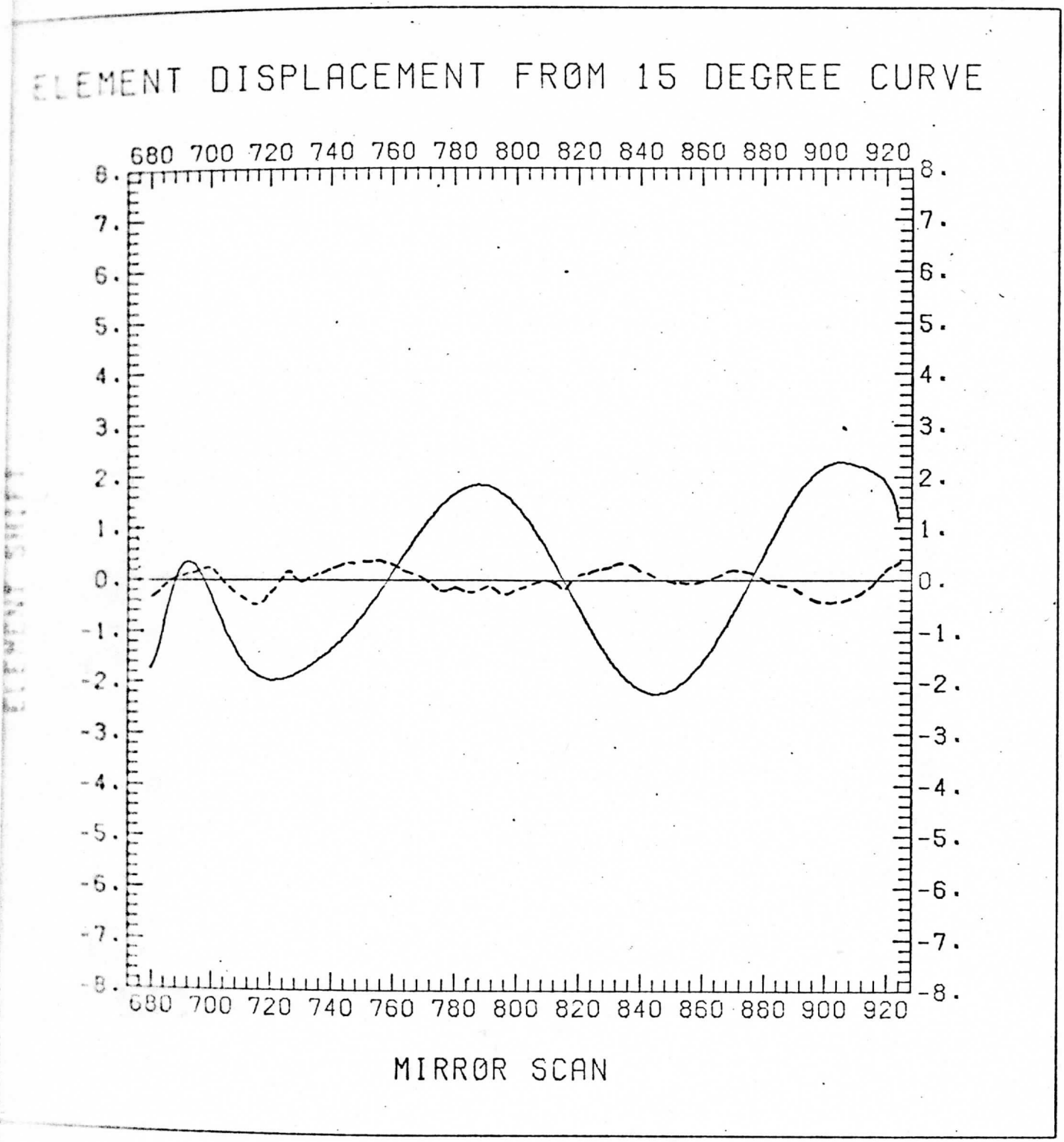

FIGURE III.4. RELATIVE ELEMENT SHIFT OF THE T_2-SSP RELATIVE to the T_1-SSP (solid curve) as a function of mirror scan number. This curve is the complement to the one in FIG. III.3. Dotted curve is pitch-angle difference between images T_1 and T_2 obtained from the attitude telemetry data plotted in FIGURE III.5. and clearly shows that these data are not able to account for the actual observed changes between ATS-6 images.

the roll-angle difference curve between T_1 and T_2 as a function of line number and the ΔE curve the pitch-angle difference curve between these two images.

(iv) The ΔL, ΔE curves are converted to look-up tables as a function of line number. Thereafter, whenever a cloud displacement is measured between the T_1-and T_2-images for the purposes of wind velocity measurements, the ΔL, ΔE values corresponding to the average scan line number of the cloud are "looked-up" and these values are subtracted off the cloud-displacement coordinates obtained by the conventional image-matching technique. The resulting modified vectors are then run through the ATS-6 model as before to convert satellite image coordinates to earth-coordinates and hence wind vectors. That this simple procedure does in fact remove the roll and pitch angle changes correctly is justified in APPENDIX B.

The method discussed above has the following advantages:

(i) attitude telemetry data are not needed;

(ii) because the method is basically a null-detection scheme, the "earth-edge" need not be defined;

(iii) distortions in the scan system do not affect the nature of the wind fields or the magnitude of the wind vectors;

(iv) landmark measurements are required for only one image in a study sequence (this statement is clarified in Appendices B and C).

The reason the method works is basically because:

(i) the ATS-6 attitude control system during the image acquisition time was good enough such that attitude changes were generally small and therefore small-angle approximations can be used in the ATS-6 navigation model with a high degree of accuracy;

(ii) attitude changes are generally slow compared to the time required to scan a line (period for an attitude oscillation cycle is on the order of 100 mirror-scan lines);

(iii) distortions in the mirror-scan nonlinearities are small and slowly varying ($\pm$2 resolution element change over 200 resolution elements along a scan line - see Appendix G);

(iv) mirror-scan nonlinearities repeat in magnitude and phase from line to line and change very slowly from image to image;

(v) yaw-angle changes are small (see Appendix E);

(vi) eccentricity of ATS-6 orbit is very small (see Appendix F).

2. Attitude Telemetry Data

FIGURES III. 5-7 show the pitch, roll and yaw-angle differences between the T_1 to T_2 images used to obtain the wind-measurements reported in this report. These attitude data were obtained from the NASA/GODDARD magnetic tapes supplied to us and represent the latest processing procedure applied to the ATS-6 telemetry data. Our June, 1976, progress report showed plots of the attitude data derived from a different processing technique which contained "saw-teeth" in the yaw and pitch data; it is evident that this artifact does not appear in the present data. That report also presented evidence that the large pitch and roll changes around Mirror Scan 200 were indeed "present" in the associated image data but that the smaller attitude angle changes seemed to have little relationship with the studied image data. The same statement is true of the present attitude data. The $T_1 - T_2$ pitch-angle differences in FIG. III.5. corresponding to the Study Area (from which the wind measurements were obtained) have been plotted in FIG. III.4. (dotted curve). Recalling that the Element Shift curve (solid line) in this figure is essentially the correct pitch-angle-difference curve,

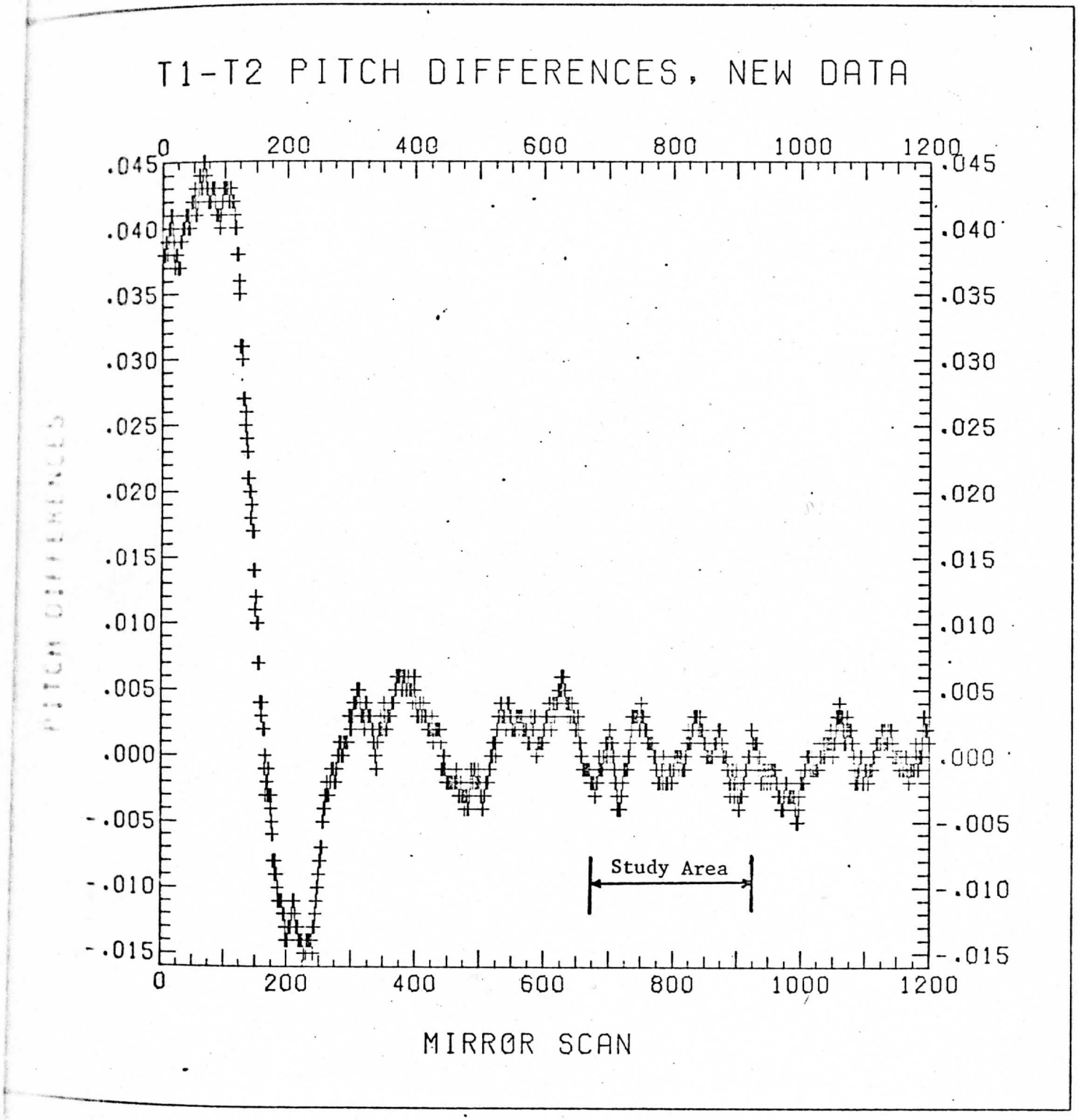

III.5. PITCH-ANGLE DIFFERENCES (DEGREES) BETWEEN ATS-6 IMAGES T_1 (164223Z) [illegible] (170658Z) attitude telemetry data from latest NASA/GODDARD tapes supplied [illegible]. Data corresponding to Study Area mirror-scan range was plotted in FIG. III.4. [illegible] first-order pitch difference results in an element difference between successive [illegible]-6 images; a 0.0083° pitch change results in a 1-element shift)

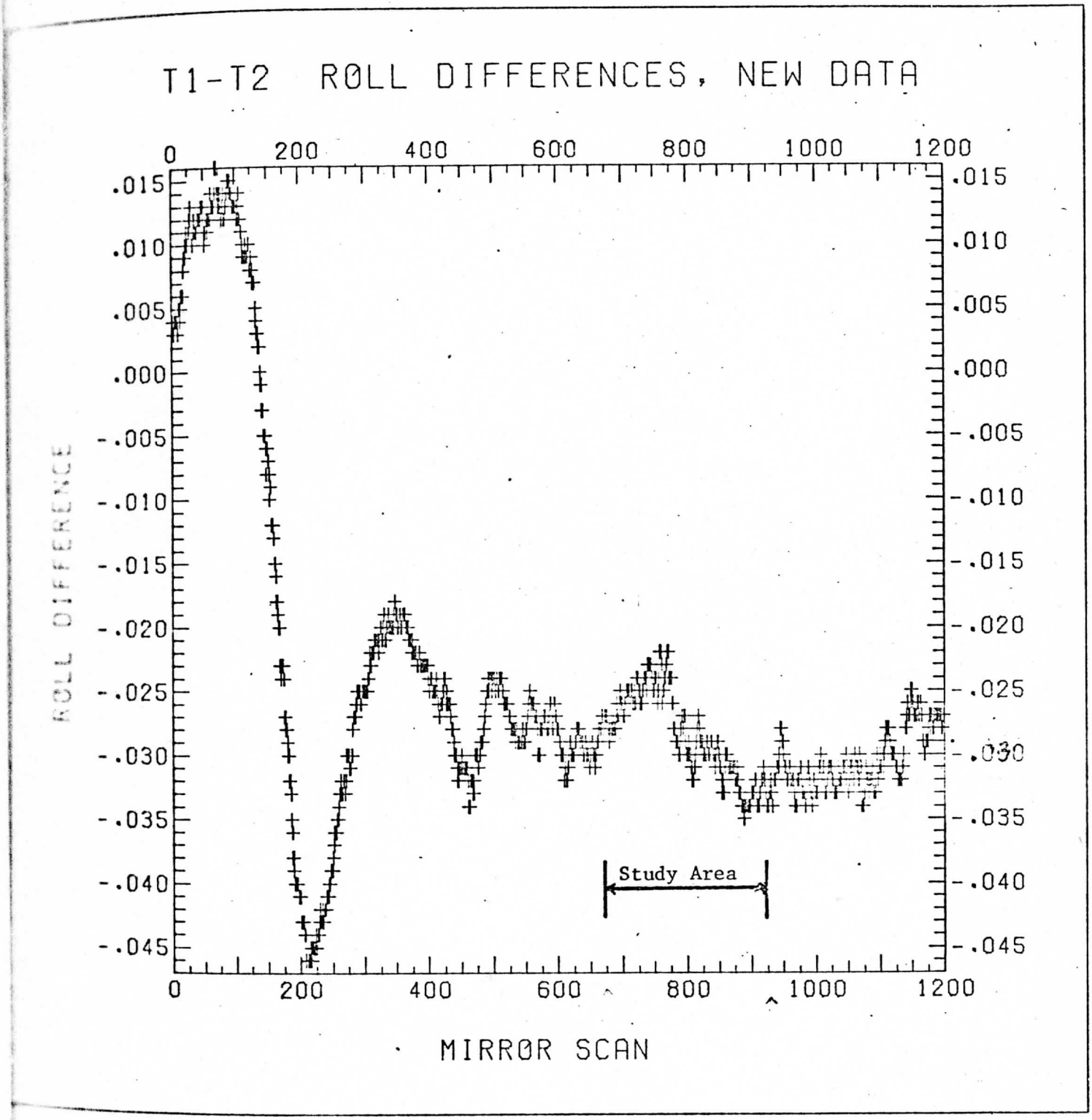

FIGURE III.6. ROLL-ANGLE DIFFERENCES (DEGREES) for same image pairs discussed in Fig. III.5.

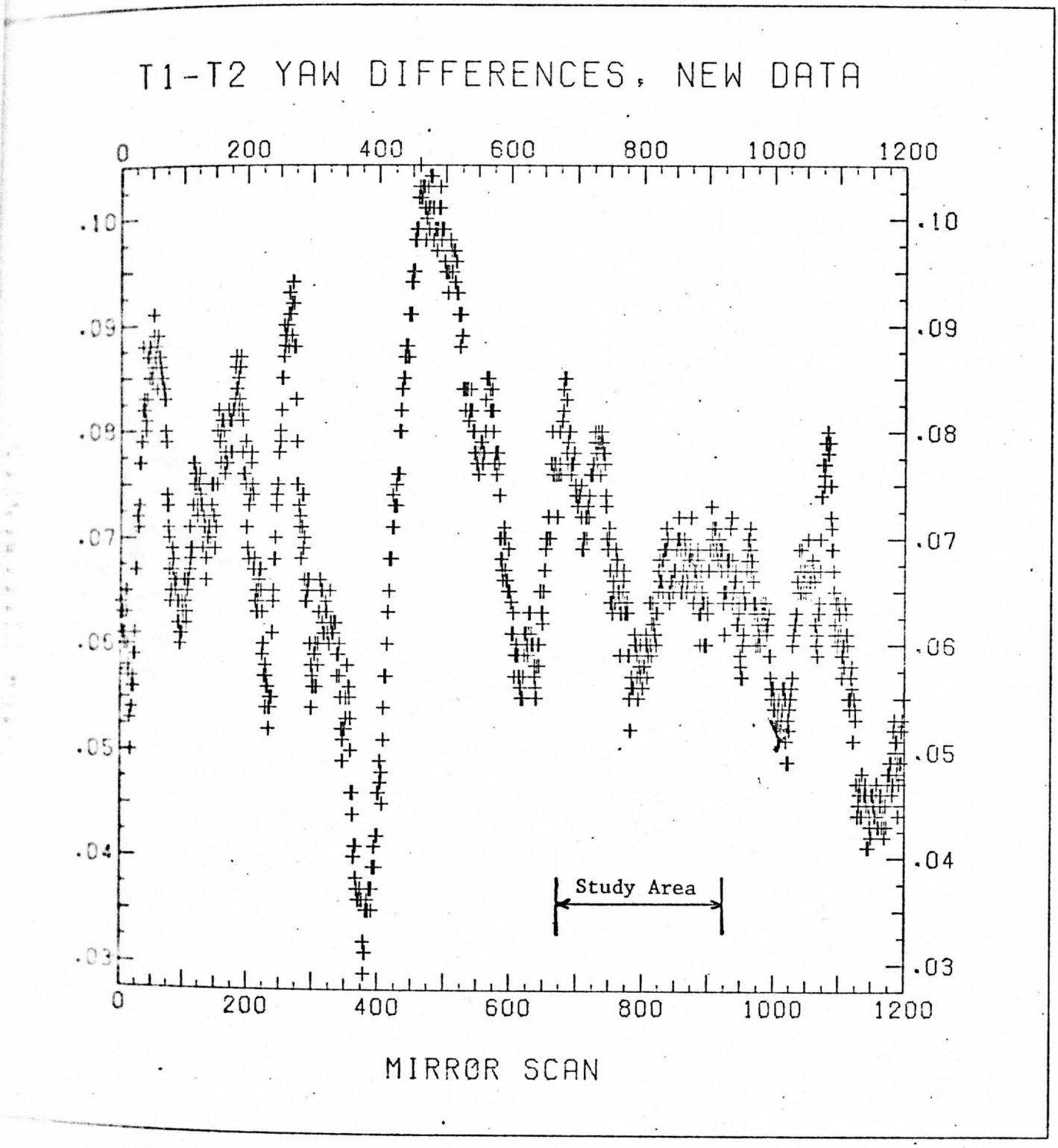

III.7. YAW-ANGLE DIFFERENCES (DEGREES) for same image pairs discussed in

it is apparent that attitude telemetry data contains no useful information for the purposes of accurate wind determination. If the dotted instead of the solid line had been used to correct for attitude changes when computing the reported winds, errors of ±5 m/sec would have resulted.

Comparing the roll-difference plot (FIG. III.6.) to the Line Shift curve (FIG. III.3.), the opposite situation exists in the sense that the roll-difference change in the Study Area interval suggested by the attitude data (about 1.5 m/sec) was not in fact observed to be the case (the Line Shift curve is essentially plot over this mirror-scan range).

). Error Analysis

There are two potential-error sources related to attitude changes which could reduce wind measurement accuracies:

(i) large yaw-angle changes (discussed in Appendix E);

(ii) large amplitude and frequency roll-angle changes occurring in the vicinity of ±100 ATS-6 scan lines about the SSP-scan line (discussed in Appendix B).

For the ATS-6 image data which is so afflicted, there is nothing that we know about that can be done to correct for these affects.

APPENDIX A. ANALYSIS OF METHOD WHICH DETERMINES ATS-6 SSP IMAGE COORDINATE DISPLACEMENTS BETWEEN SUCCESSIVE IMAGES RESULTING FROM ATTITUDE CHANGES

As shown in Section III, the ATS-6 attitude telemetry data time series was shown to be inadequate for the purpose of accurate wind measurements. This appendix presents an analysis of the technique used to calculate the ATS-6 Subsatellite Point (SSP) image coordinate changes between successive images (shown in FIGS. III.3. and III.4.) resulting from attitude changes during the image-scan time. Appendix B shows how these measurements are used to account for the attitude changes in the process of computing accurate cloud displacements.

1. Method

Let T_1, T_2 designate two successive ATS-6 data images where T_1 is the "earlier" of the two images and (L_c, E_c) (Line scan and Element numbers) are its SSP image coordinates (FIG. A.1.) determined from the ATS-6 navigation model. Let (L,E) be the T_1 image coordinates for a point on the right earth edge and ΔE_R, ΔE_L the measured displacements along line L of the Right and Left T_2-earth edges relative to the T_1 earth edges. (These measurements are obtained in practice on McIDAS using the infrared ATS-6 data images and an image-matching technique which is constrained to measure displacements of the earth edge only along a scan line. It is worth emphasizing that the image-matching method indeed measures displacements of the geometrical earth edge and not features near it - such as clouds.* This is not surprising since the greatest contrast is between earth and space - not within features near the earth's edge.)

The object, then, is to compute the displacement coordinates $(\Delta L, \Delta E)$ of the T_2-SSP relative to the T_1-SSP at line L using the measured values of $\Delta E_R, \Delta E_L$.

*See added note at the end of this appendix.

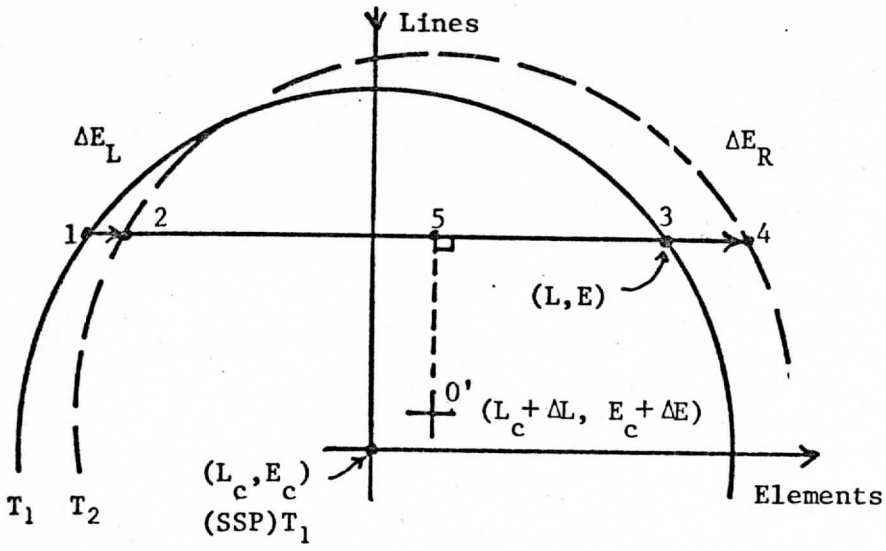

FIGURE A.1. Earth-edge Displacement Measurement Geometry

Let points 1-5 be on line L at the earth edges indicated in the figure, and points 0 and 0' the T_1-SSP and T_2-SSP. Furthermore, point 5 is the nadir point for the T_2-chord coinciding with line L, and both T_1- and T_2-earth circles have equal radii a.

Letting $\overline{P_i - P_j}$ be the distance (always non-negative) between points i and j, $\Delta L, \Delta E$ can be derived from two simple geometrical identities:

The first is

$$\overline{P_4 - P_5} = \overline{P_5 - P_2} \text{ , or}$$

$$(E + \Delta E_R) - (E_c + \Delta E) = (E_c + \Delta E) - (2E_c - E + \Delta E_L) \text{ ,}$$

solving for ΔE,

$$\Delta E = (\Delta E_R + \Delta E_L)/2 \text{ .} \qquad (1)$$

The second identity is

$$\overline{P_4 - P_2} - \Delta E_R = \overline{P_3 - P_1} - \Delta E_L \text{ , where} \qquad (2)$$

$$\overline{P_4 - P_2} = 2\sqrt{(\overline{P_4 - P_{0'}})^2 - (\overline{P_5 - P_{0'}})^2}$$

$$= 2\sqrt{(\overline{P_3 - P_0})^2 - (\overline{P_5 - P_{0'}})^2}$$

$$= 2\sqrt{(L - L_c)^2 + (E - E_c)^2 - [L - (L_c + L)]^2} \text{ , and} \qquad (3)$$

$$\overline{P_3 - P_1} = 2(E - E_c) \text{ .} \qquad (4)$$

Substitution of (3) and (4) into (2) and rearranging yields

$$\delta = \sqrt{X^2 + Y^2 - (Y - \Delta L)^2} - X \text{ , where} \qquad (5)$$

$$\delta = (\Delta E_R - \Delta E_L)/2$$

$$X = E - E_c$$

$$Y = L - L_c \text{ .}$$

Since δ is obtained from the $\Delta E_R, \Delta E_L$ measurements and (L,E), (L_c,E_c) are known, ΔL can be solved for (5) to yield

$$\Delta L = Y \pm \sqrt{RAD} \text{ , where} \qquad (6)$$

$$RAD = Y^2 - 2 X \delta - \delta^2 \text{ .}$$

The choice of sign in (6) is determined by substituting the expression for δ in Eq. (5) in RAD; the result is

$$\begin{aligned} \Delta L = Y \pm \sqrt{(Y - \Delta L)^2} &= Y + \sqrt{RAD} \text{ , } Y > \Delta L \\ &= Y - \sqrt{RAD} \text{ , } Y < \Delta L \text{ .} \end{aligned} \qquad (7)$$

The peculiar condition implied by (7) that ΔL must be known before ΔL can be calculated is really not a problem since generally ΔL is small ($\pm$ 5 lines) and $|Y|$ is usually $>>$ $|\Delta L|$. For most cases then the conditions are

$$\Delta L = Y \pm \sqrt{RAD} \text{ , } Y \gtrless 0 \text{ ,} \qquad (8)$$

$$RAD = Y^2 - 2 X \delta - \delta^2 \text{ .}$$

For the case where $|Y|$ approachs (ΔL) in value there are other problems; these are discussed at the end of this appendix.

Equations (1) and (8), then, define the displacement in image coordinates of the T_2-SSP relative to the T_1-SSP for line L. By repeating this entire process for other scan lines the SSP-shifts $(\Delta L, \Delta E)$ as function of T_1-line position are obtained. In practice the right and left earth-edge displacements are first measured over the entire range of scan lines of interest. Curves are then separately fit to the right and left edges measurements (see FIGS. III.1. and III.2.) resulting in a ΔE_R vs L and a ΔE_L vs L curve over the scan-line range of interest. The curve values themselve are then used in (1) and (8) to compute the $\Delta L, \Delta E$ curves shown in FIGS. III.3. and III.4.

2. Error Analysis

The magnitude of the errors associated with the displacement coordinates $(\Delta L, \Delta E)$, denoted by $(\Delta(\Delta L), \Delta(\Delta E))$, depend on the accuracy to which the horizontal earth-edge displacements can be measured and the location on the image (i.e. polar, equatorial) where $(\Delta L, \Delta E)$ are being computed.

For regions near the poles, the slope of the earth edge approaches zero and the "edge" covers an increasing number of elements for each scan line. The horizontal image matching accuracy does not noticeably degrade until the slope is below 45°, nominally corresponding to a latitude of 50°. However in this region of the image, the location inaccuracies resulting from foreshortening of features on the earth is severe enough that wind measurements are generally not made at these higher latitudes. Thus the error in $\Delta E(\Delta(\Delta E))$ associated with the study regions of interest (between $\pm$ 50° latitude) is the error associated with the difference in the earth-edge displacement curves shown in FIGURES III.1. and III.2. From (1) and (5)

it is seen that $\Delta(\Delta E) \cong \Delta\delta$ and this average error as seen in these figures and also suggested by the accuracy in the resulting wind measurements is estimated to be about .1 pixel; thus, $\Delta(\Delta E) \cong \Delta\delta$ = .1 pixel. (9)

The error $\Delta(\Delta L)$, on the other hand, increases in size for lines near the SSP (nominally the equator).

Letting

$$a^2 = (L - L_c)^2 + (E - E_c)^2 = (\text{radius of earth-image})^2 = (1044 \text{ pixels})^2$$

$$b^2 = (Y - \Delta L)^2;\ Y = L - L_c$$

$\Delta\delta$ = measurement error,

then from (8)

$$\Delta(\Delta L) = \Delta L(\delta + \Delta\delta) - \Delta L(\delta)$$

$$= \pm \left[\sqrt{RAD(\delta + \Delta\delta)} - \sqrt{RAD(\delta)}\right] \text{ for } b \lesssim 0$$

$$\cong \pm \left[\sqrt{b^2 - 2\Delta\delta(a^2 - b^2)^{1/2}} - b\right] . \quad (10)$$

The region in which equation (8) for the computation of ΔL breaks down is when the value of L (and hence b) is such that the expression of the radical in (8) is zero, i.e.

Region for which (8) is invalid occurs when:

$$|b| = |L - L_c - \Delta L| \lesssim \sqrt{2a\Delta\delta} = 14 \text{ pixels} , \quad (11)$$

where the assumption $b^2 << a^2$ was made (generally $|\Delta L|$ does not exceed 5 scan lines, thus as L approachs L_c, b^2 gets very small compared to a^2).

For $b^2 \gtrsim 10\ (2a\Delta\delta)$, (10 reduces to

$$\Delta(\Delta L) \cong \pm \sqrt{a^2/b^2 - 1} , \ b \lesssim 0 . \quad (12)$$

Values of $\Delta(\Delta L)$ computed for various values of b using (11) appear in the table below.

Approximate number of lines from SSP-line $\lvert b \rvert$	Mean-maximum error (lines) $\lvert \Delta(\Delta L) \rvert$ †
50	2.1
100	1.0
200	0.5
300	0.3
400	0.2
500	0.2
600	0.1

TABLE A.1. Line-Shift Errors as a Function of Line Number for an earth-edge displacement error of 0.1 pixel.

†Visible image lines (2 visible lines equals 1 ATS-6 mirror-sweep line).

This table and TABLE D.1. indicate that in the range of $\pm$ 200 lines ($\pm$ 100 ATS-6 scan lines) about the SSP-line that wind-measurement errors would exceed 1 m/sec for a 3-image study sequence if nothing were done to reduce the $\Delta(\Delta L)$ errors. Fortunately, the ΔL vs L curve (FIG. III.3.) is a slowly varying curve whose amplitude fluctuations tend to be small; thus the ΔL vs L curve can be interpolated across the SSP region from the curves derived on either side of it.

---

*Note added from p. A-1. That the image-matching technique measured earth-edge and not cloud displacements on the earth edge was checked by two methods: 1) earth-edge measurements were made on the earth's limb using the visible imagery and compared to those measurements made from the associated infrared imagery covering the same portion of the earth edge; 2) the infrared digital images were remapped so that brightness values above and below threshold values determined from the earth-edge values were set equal to a constant leaving only the earth edge values unchanged. (The unchanged earth edge image was about 3 pixels wide or 15 km at the equator). Earth edge measurements were made and compared to the measurements made from the unmapped data. In both tests the resulting comparison curves were identical.

APPENDIX B. ANALYSIS OF ALGORITHM WHICH ACCOUNTS FOR RELATIVE ATTITUDE CHANGES IN SUCCESSIVE ATS-6 DATA IMAGES USING EARTH-EDGE SHIFT MEASUREMENTS

This appendix provides a semi-rigorous analysis of the algorithm used to account for the relative attitude changes in a sequence of ATS-6 data images using the earth-edge measurements derived by the technique discussed in the main portion of the report and APPENDIX A. In effect, this appendix shows why the algorithm "works"; the following appendices discuss in more detail the limitations of and the errors associated with this method.

Consider a sequence of n ATS-6 images designated by T_1, T_2, ... T_n, from which the displacements in earth coordinates of a feature (cloud) between successive images are to be determined. Let

(L_i, E_i) = image coordinates (Line, Element) of the cloud feature for the T_i^{th} image,

$\hat{r}_{PFi} = \hat{r}_{PF}(L_i, E_i)$ = unit pointing vector in Picture Frame coordinates derived from (L_i, E_i) using the ATS-6 scan-camera geometry,

$\hat{r}_{LVi}$ = unit Local Vertical pointing vector associated with $\hat{r}_{PFi}$,

R_i = 3x3 rotation matrix which transforms <u>without error</u> r_{LVi} into $\hat{r}_{PFi}$ at the time the feature was scanned, i.e.

$$\hat{r}_{PFi} = R_i \, \hat{r}_{LVi} \, . \tag{1}$$

1. A Two-Image Sequence

Consider now the first two images T_1, T_2 in the sequence whose relationship between LV and PF coordinates are given by

$$\hat{r}_{PF1} = R_1 \, \hat{r}_{LV1} \tag{2}$$

$$\hat{r}_{PF2} = R_2 \, \hat{r}_{LV2} \, . \tag{3}$$

The relationship of the cloud feature in LV coordinates for image T_2 can be related to T_1 as follows:

$$\hat{r}_{LV2} = \hat{r}_{LV1} + \Delta\vec{r}_{LV}(\Delta T_{12}) \ , \tag{4}$$

where $\Delta\vec{r}_{LV}$ is the displacement of the cloud in LV coordinates from T_1 to T_2 and results from two effects:

(i) apparent change in the earth's orientation over the time interval ΔT_{12} caused by a non-zero angle of inclination in the satellite's orbit (the eccentricity of the ATS-6 orbit was so small ($\sim 10^{-4}$) that no significant change in angular size occurs - see Appendix F);

(ii) motion of the cloud relative to the earth's surface.

Now the orientation of the earth relative to the LV frame depends only on the orbit and the earth's position relative to celestial coordinates; thus if $\hat{r}_{LV1}$ and $\hat{r}_{LV2}$ were accurately known, the displacement of the cloud over the time interval associated with these two vectors could be calculated with an accuracy limited only by the equations describing the dynamical relationship between the satellite orbit and the earth's position relative to celestial coordinates. It is assumed that for ATS-6 that this transformation produces negligible error.

Returning to equations (2) and (3), the rotation matrices R_1, R_2 differ from each other slightly because of an attitude change of the PF frame relative to the LV frame between T_1 and T_2; they are related to each other by an infinitesimal rotation $I + E_{12}$ where I is the unit matrix and E_{12}, an antisymmetic matrix whose elements are the small-angle differences between the PF axes at times T_1 and T_2. Thus

$$R_2 = (I + E_{12})\, R_1 \; ; \tag{5}$$

substituting (4) and (5) in (3) and expanding

$$\hat{r}_{PF2} = R_1 \hat{r}_{LV1} + E_{12} R_1 \hat{r}_{LV1} + R_1 \Delta\vec{r}_{LV}(\Delta T_{12}) + E_{12} R_1 \Delta\vec{r}_{LV}(\Delta T_{12}) \tag{6}$$

The first term on the RHS of (6) is $\hat{r}_{PF1}$, the last term is negligible ($\sim 10^4$ times smaller than the first order terms), the second term is the change in PF coordinates due to an attitude change and the third term is the change in PF coordinates due to the two changes in the LV frame discussed above. Using (4) to combine the first and third terms, equation (6) then can be rewritten as

$$\hat{r}_{PF2} = R_1 \hat{r}_{LV2} + E_{12} \hat{r}_{PF1} \; . \tag{7}$$

Comparison of (7) with (2) implies that if E_{12} and R_1 were known, $\hat{r}_{LV1}$ and $\hat{r}_{LV2}$ - and therefore the cloud displacement - could be computed with a high degree of accuracy.

A good approximation to E_{12} is obtained from the earth-edge displacement measurements which provide the displacement in image coordinates $\Delta L_{12}(L)$, $\Delta E_{12}(L)$ of T_2 relative to T_1 as a function of line number L.† The line shift ΔL_{12} is proportional to a small change in roll ΔR_{12} about the PF-X axis and the element shift is proportional to small changes in pitch ΔP_{12} about the PF-Y axis, i.e.

$$\Delta L_{12} = \Delta R_{12}/\rho \; , \tag{8a}$$

$$\Delta E_{12} = \Delta P_{12}/\rho \; , \tag{8b}$$

where ρ is the angular size of a pixel = 1.45×10^{-4} radians.

Letting $\hat{r}_{PF1} = [X, Y, Z]^T$ where T is the transpose, the explicit form of E_{12} and the last term in (7) is

†These displacement measurements are obtained by the method discussed in Sec. III. and Appendix A; curves showing the displacements $\Delta L, \Delta E$ as a function of L are shown for one image pair in FIGS. III.3. and III.4.

$$E_{12}\hat{r}_{PF1} = \begin{bmatrix} 0 & 0 & \Delta P \\ 0 & 0 & \Delta R \\ -\Delta P & -\Delta R & 0 \end{bmatrix} \begin{bmatrix} X \\ Y \\ Z \end{bmatrix}$$

$$= [\Delta PZ,\ \Delta RZ,\ -\ (\Delta PX + \Delta RY)]^T, \qquad (9)$$

where it is understood that ΔR, ΔP refer to the T_1 to T_2 changes in attitude at the times the cloud was scanned.

Note E_{12} contains no non-zero yaw angle element (small rotation about the axis passing through the image SSP) since there is no way that the earth-edge displacement measurement technique can provide this angle; however, the analysis given in Appendix E shows that the effect on the accuracy of wind measurements (displacements) for yaw changes is generally small. Analysis of landmark measurements and the ATS-6 wind sets shown in this report, indicate that for the data images studied thus far, the yaw changes are negligible.

With E_{12} and hence the last term in (7) determined, equation (7) can be rewritten as

$$\hat{r}'_{PF2} = \hat{r}_{PF2} - E_{12}\hat{r}_{PF1} = R_1\hat{r}_{LV2}\ , \qquad (10)$$

where $\hat{r}'_{PF2}$ is interpreted as the T_2 cloud pointing vector with the attitude changes removed.

2. Computing $\hat{r}'_{PF2}$ in Practice

Cloud displacement measurements and computation of $\hat{r}'_{PF2}$ is accomplished as follows:

(1) the T_1 image coordinates (L_1, E_1) of the cloud are recorded,

(2) the total displacement of the cloud in image coordinates $(\Delta L^T, \Delta E^T)$ from T_1 to T_2 are measured on McIDAS using an image matching technique,

(3) from previously determined earth-edge displacement parameters, the displacement coordinates ΔL_{12}, ΔE_{12} due to relative attitude changes are computed and subtracted from ΔL^T, ΔE^T. These differences are added to L_1, E_1 and the associated PF vector computed. That this vector is a good approximation of $\hat{r}'_{PF2}$ is shown below.

By definition,

$$\hat{r}_{PF1} = \hat{r}_{PF}(L_1, E_1) \tag{11}$$

$$\hat{r}_{PF2} = \hat{r}_{PF}(L_1 + \Delta L^T, E_1 + \Delta E^T) = \hat{r}_{PF}(L_2, E_2) \tag{12}$$

Expanding $\hat{r}_{PF}(L_1 + \Delta L^T - \Delta L_{12}(L_2), E_1 + \Delta E^T - \Delta E_{12}(L_2))$ about $(L_1 + \Delta L^T, E_1 + \Delta E^T)$ keeping first order terms, we have

$$\hat{r}_{PF}(L_1 + \Delta L^T, E_1 + \Delta E^T) - \frac{\partial}{\partial L} \hat{r}_{PF}(L_2, E_2)\, \Delta L_{12} - \frac{\partial}{\partial E} \hat{r}_{PF}(L_2, E_2)\, \Delta E_{12} . \tag{13}$$

From the geometry of the ATS-6 scan-camera,

$$\hat{r}_{PF} = [-\cos\lambda\sin\delta,\ -\sin\lambda,\ \cos\lambda\cos\delta]^T \tag{14}$$
$$= [X,\ Y,\ Z]^T$$

where

$\lambda = (L_c - L)\rho$ = mirror step angle,

$\delta = (E_c - E)\rho$ = mirror sweep angle,

(L_c, E_c) = image center line and element value,

ρ = angular size of a line or element.

Taking the partials of $\hat{r}_{PF}$ in (14) with respect to L,E, and retaining first order terms with the partials evaluated at (L_2, E_2):

$$\frac{\partial}{\partial L}\hat{r}_{PF}\,\Delta L_{12} + \frac{\partial}{\partial E}\hat{r}_{PF}\,\Delta E_{12}$$

$$= [0,\ PZ,\ -PY]^T \Delta L_{12} + [PZ,\ 0,\ -PX]^T \Delta E_{12}\ , \qquad (15)$$

substituting (8a) and (8b) into the above expression and adding the two vectors in (15) yields

$$[Z\Delta P_{12},\ Z\Delta R_{12},\ -(X\Delta P_{12} + Y\Delta R_{12})]^T\ ,$$

which is equivalent to (9); therefore (15) is the same as $E_{12}\hat{r}_{PF1}$. Since the first term in (13) is $\hat{r}_{PF_2}$, we have

$$\hat{r}_{PF}(L_1 + \Delta L^T - \Delta L_{12}(L_2),\ E_1 + \Delta E^T - \Delta E_{12}(L_2)) \doteq$$

$$\hat{r}_{PF_2} - E_{12}\hat{r}_{PF} = \hat{r}'_{PF_2} \quad \text{by} \qquad (16)$$

comparison with (10). Thus the method discussed above correctly yields $\hat{r}'_{PF_2}$.

3. Transforming PF to LV coordinates

With the attitude changes between T_1 and T_2 removed, we have

$$\hat{r}_{PF1} = R_1\hat{r}_{LV1} \qquad (17)$$

$$\hat{r}'_{PF_2} = R_1\hat{r}_{LV2} \quad \text{(see (10))} \qquad (18)$$

Let $\overline{R}$ be the transformation from LV to PF coordinates derived from T_1 landmark measurements in a least squares sense assuming a constant attitude over the time interval the T_1 landmarks were scanned, i.e. $\overline{R}$ is a constant matrix. $\overline{R}$ then will differ slightly from R_1 due to small

attitude changes over the T_1 scan time and, in addition, will differ from R_1 (assumed to be the error-free transformation) due to mirror scan nonlinearities. Similarly, as above, we can relate $\bar{R}$ to R_1 by an infinitesimal transformation

$$\bar{R} = R_1 \ (I - e) \ , \tag{19}$$

where e is the infinitesimal antisymmetric error matrix which is a function of line and element. It is important to realize that the elements of e contain absolute errors (Appendix C) which the ATS-6 model cannot account for. However, our previous work using landmark measurements has provided us with bounds on these errors and the rate at which they change as a function of image coordinates. The worst-case estimates correspond to about $\pm$ 2.5 pixels ($\pm$ 3.6 $\times 10^{-4}$ radians). The errors tend to be oscillatory as a function of line or element position with a period of 100 to 200 pixels. Thus for typical feature displacement measurements (corresponding to tens of pixels), e can be considered to be a constant locally. (It would be appropriate to remind the reader at this point that the absolute mirror scan nonlinearities as a function of image coordinates repeat from image to image.)

Taking the transpose of (19) and operating on (17) and (18)

$$\hat{r}'_{LV1} = \bar{R}^T \hat{r}_{PF1} = (I + e) R_1^T R_1 \hat{r}_{LV1} = \hat{r}_{LV1} + \vec{r}_e \tag{20a}$$

$$\hat{r}'_{LV2} = \bar{R}^T \hat{r}'_{PF2} = (I + e) R_1^T R_1 \hat{r}_{LV2} = \hat{r}_{LV2} + \vec{r}_e \ , \tag{20b}$$

where

$$\vec{r}_e = e \hat{r}_{LV} \ . \tag{21}$$

Application of $\bar{R}$ then, results in the correct LV vectors to within the same additive vector constant. It is shown in Appendix C that this constant has a negligible effect in computing cloud velocities or displacements.

addition location errors on the earth due to $\vec{r}_e$ is given in this ppendix.

. General Case of n-image Sequence

The case for images T_1, T_2, ... T_n is simply a generalization of the -image case. The error-free LV to PF frame matrix for T_i can be related to R_1 by the image pair relative-attitude transformation matrices $E_{i,i+1}$ where

$$R_n = (I + E_{n-1,n}) \cdots (I + E_{23})(I + E_{12})R_1$$

$$= \left(I + \sum_{i=1}^{n-1} E_{i,i+1}\right)R_1 , \qquad (22)$$

where only first order terms are retained. Thus the analog to (10), generalized to n images, is

$$\hat{r}'_{PFn} = \hat{r}_{PF} - \left(\sum_{i=1}^{n-1} E_{i,i+1}\right)\hat{r}_{PF1} = R_1 \hat{r}_{LVn} ,$$

where in practice $\hat{r}'_{PFn}$ is computed by evaluating the expression

$$\hat{r}'_{PFn} = \hat{r}_{PF}\left(L_n - \sum_{i=1}^{n-1} \Delta L_{i,i+1}(L_{i+1}),\ E_n - \sum_{i=1}^{n-1} \Delta E_{i,i+1}(L_{i+1})\right) \qquad (23)$$

where $L_{i,i+1}(L_{i+1})$, $E_{i,i+1}(L_{i+1})$ are evaluated from the T_i to T_{i+1} earth-edge displacement measurements evaluated at L_{i+1}, where L_{i+1} is the T_{i+1} line number of the "center of gravity" of the feature being tracked.

Application of (19) to the $\hat{r}'_{PFi}$ results in

$$\hat{r}'_{LVi} = \hat{r}_{LVi} + \vec{r}_e \qquad i = 1, 2, \ldots n \ . \qquad (24)$$

APPENDIX C. EFFECT OF ABSOLUTE ATTITUDE ERROR ON THE ACCURACY OF WIND MEASUREMENTS AND FEATURE LOCATION

As discussed in the main body of the report and Appendix B, the transformation from the ATS-6 image frame (PF) to the Local Vertical (LV) contains an absolute error term because of landmark measurement errors and absolute mirror scan nonlinearities. This means that the computed location in earth coordinates of a feature on the ATS-6 image will be in error. Because this error is the same for successive images and changes slowly as a function of image position compared to features such as clouds "moving" on these successive images, the error of the measured displacements and consequently the errors in the wind measurements will be negligible but the errors in absolute location resulting from the absolute attitude uncertainty error will become more important. The purpose of this appendix is to compute the velocity and location errors as a function of angle measured from the SSP due to the absolute attitude error.

From eqs. (4) and (20) in Appendix B,

$$\hat{r}'_{LV}(t_1) = \hat{r}_{LV}(t_1) + \vec{r}_e \qquad (1)$$

$$\hat{r}'_{LV}(t_2) = \hat{r}_{LV}(t_1) + \Delta\vec{r}_{LV}(t_{12}) + \vec{r}_e \qquad (2)$$

where

$\hat{r}_{LV}(t_1)$ = correct LV unit vector which points from the satellite to a cloud at time t_1

$\hat{r}'_{LV}(t_1)$ = computed LV unit pointing vector for cloud at time t_1

$\vec{r}_e$ = vector error resulting from absolute attitude error

$\hat{r}'_{LV}(t_2)$ = computed LV unit pointing vector for cloud at t_2

$\Delta\vec{r}_{LV}(\Delta t_{12})$ = change in computed pointing vectors due to clouds motion in the time interval Δt_{12} from t_1 to t_2,

where $\|\vec{r}_e\|$, $\|\Delta\vec{r}_{LV}\| << \|\hat{r}_{LV}(t_i)\| = 1$.

The geometrical relationship of these terms is shown (greatly exaggerated) in Figure C.1. where it is assumed all vectors are coplanar. Figure C.2. shows how these vectors relate to the satellite/earth system.

In Figure C.2. the following are defined:

P = point on earth's surface of cloud at time t_1

θ = angle at earth center between SSP-Satellite line and cloud

ϕ = angle between SSP-Satellite line and $\hat{r}_{LV}(t_1)$

R = earth radius = 6378 km

K = 6.61 for geosynchronous satellite.

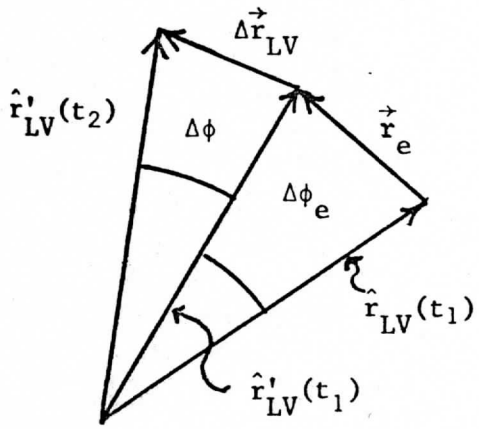

FIGURE C.1. Geometrical Relationship Among Pointing Vectors

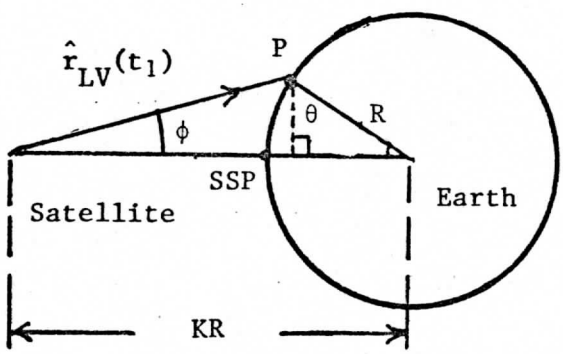

FIGURE C.2. Satellite/Earth Geometry

Clearly the greatest error resulting from $\vec{r}_e$ occurs when it lies in the plane formed by $\hat{r}'_{LV}(t_1)$ and $\hat{r}'_{LV}(t_2)$ and points in the same direction as $\Delta\vec{r}_{LV}$. Since an upper bound on the errors is desired all subsequent analysis will be confined to a plane and it will be assumed that $\Delta\vec{r}_{LV}$ and $\vec{r}_e$ point in such a direction as to increase ϕ. With these stated conditions the computed velocity $\vec{V}$ can be treated as a scalar.

The correct velocity V of the cloud from times t_1 to t_2 at point P is given by

$$V = C[\theta(\phi + \Delta\phi) - \theta(\phi)] \ , \tag{3}$$

where

$C = R/\Delta t_{12}$

$\Delta\phi = \|\Delta\vec{r}_{LV}\|$ = change in ϕ due to cloud motion

$\theta(\phi)$ = value of θ for a given value of ϕ to be derived later on.

Assuming $\Delta\phi << \phi$ and expanding θ about ϕ, keeping first-order terms, (3) becomes

$$V \cong C\ \theta'\ \Delta\phi, \ \theta' = d\theta/d\phi \ . \tag{4}$$

The error in V, ΔV resulting from $\vec{r}_e$ is

$$\begin{aligned} \Delta V &= C\{[\theta(\phi + \Delta\phi + \Delta\phi_e) - \theta(\phi + \Delta\phi_e)] - [\theta(\phi + \Delta\phi) - \theta(\phi)]\} \\ &\cong C[\theta'(\phi + \Delta\phi_e) - \theta(\phi)]\ \Delta\phi \\ &\cong C\ \theta''(\phi)\ \Delta\phi_e\ \Delta\phi \ , \end{aligned} \tag{5}$$

where (5) was expanded as above keeping first-order terms and

$$\theta''(\phi) = \frac{d^2\theta}{d\theta^2}\Big]_\phi$$

$\Delta\phi_e = \|\vec{r}_e\|$ = error in ϕ resulting from vector error $\vec{r}_e$.

At this point it is convenient to compute θ', θ''. From Fig. C.2. is easily seen that

$$\tan\phi = \frac{\sin\theta}{K - \cos\theta} \quad . \tag{6}$$

From (6) θ', θ'' are computed and (6) is used to eliminate ϕ, thus:

$$\theta'(\theta) = \frac{(K - \cos\theta)^2 + \sin^2\theta}{K\cos\theta - 1} \quad , \tag{7}$$

$$\theta''(\theta) = \theta'(\theta)\left[\frac{K\sin\theta\ (2 + \theta'(\theta))}{K\cos\theta - 1}\right] \quad , \tag{8}$$

where $\theta' = \frac{d\theta}{d\phi}$, $\theta'' = \frac{d\theta'}{d\phi}$.

The fractional error in velocity $\Delta V/V$ as a function of θ can be expressed using (4), (5), (7) and (8) as

$$\frac{\Delta V}{V} = \frac{\theta''(\theta)}{\theta'(\theta)}\,\Delta\phi_e = \left[\frac{K\sin\theta\ (2 + \theta'(\theta))}{K\cos\theta - 1}\right]\Delta\phi_e \tag{9}$$

Values of $\Delta V/V$ can be computed as a function of θ when $\Delta\phi_e$ is assigned a value. As discussed before the worst-case estimate in the absolute attitude error is

$$\pm\ 2.5 \text{ pixels} = \pm\ 2.5 \text{ pixels (1/120 ATS-6 pixels/deg)}$$

$$= \pm\ .021° = \pm\ 3.6 \times 10^{-4} \text{ radians.}$$

Using $\Delta\phi_e = 3.6 \times 10^{-4}$ radians in (9), we find that for $\theta = 60°$,

$$\Delta V/V < .02 \ .$$

Since $\Delta V/V$ increases with increasing angle θ and recalling that almost all wind-velocity measurements are confined to study areas within an angle θ of 50° to 55°, we conclude that the effect on wind velocity measurement errors due to absolute attitude-angle uncertainty errors is entirely negligible.

Location Errors

The absolute location error S in earth coordinates (degrees and kilometers) is

$$S(km) = R[\theta(\phi + \Delta\phi_e) - \theta(\phi)]$$

$$\cong R\,\theta'(\theta)\,\Delta\phi_e\,, \qquad (10)$$

$$S(degrees) \cong \theta'(\theta)\,\Delta\phi_e\,. \qquad (11)$$

Using the values R = 6378 km and $\Delta\phi_e = 3.6 \times 10^{-4}$ and the expression for $\theta'(\theta)$ given by (7), and substituting in (10) and (11) we arrive at the following table.

Angle	Absolute Location Error for ± 2.5 Pixel Uncertainty	
θ(degrees)	± ΔS (degrees)	± ΔS (kilometers
0	0.12	13.0
10	0.12	13.3
20	0.13	14.4
30	0.15	16.3
40	0.18	19.7
50	0.23	25.8
60	0.34	38.6

TABLE C.1. Absolute Location Errors as a Function of Angular Distance from the SSP. These errors result from absolute landmark measurement and mirror scan nonlinearity errors.

APPENDIX D. PIXEL MEASUREMENT ACCURACY REQUIRED FOR ACCURATE WIND MEASUREMENTS

This appendix estimates the image-matching accuracy required between successive ATS-6 images to obtain wind-speed measurement accuracy to within $\pm$ 1 m/s.

Referring to Fig. C.2. in Appendix C, the following are defined (it is assumed that the image-matching error angles lie in the plane of the page).

$\Delta\phi$ = pointing angle error resulting from image-matching error between two successive ATS-6 images

ΔP = pointing error in pixels corresponding to $\Delta\phi$

Δt = time difference between two successive ATS-6 image (24.6 min)

ΔV = velocity measurement error resulting from $\Delta\phi$

R = radius of earth (6378 km)

K = 6.61 for a geosynchronous satellite.

An image-matching error in $\Delta\phi$, results in a corresponding error in $\Delta\theta$ and hence in the velocity V as follows:

$$\Delta V = R\,\frac{K\Delta\phi}{\Delta t} = R\,\frac{\Delta\theta}{\Delta t} \quad \text{at the SSP,}$$

and

$$\Delta V = \frac{R}{\Delta t}\left.\frac{d\theta}{d\phi}\right|_{\theta} \quad \text{for an arbitrary } \theta, \tag{1}$$

where

$$\Delta\phi = \frac{\Delta P \text{ (pixels)}}{120\left(\frac{\text{ATS-6 pixels}}{\text{degree}}\right)}\,\frac{\pi}{180}\,\frac{\text{rad}}{\text{deg}}\,, \tag{2}$$

$$\left.\frac{d\theta}{d\phi}\right|_{\theta} = \frac{(K - \cos\theta)^2 + \sin^2\theta}{K\cos\theta - 1} \quad \text{eq. (7), Appendix C} \tag{3}$$

Substitution of (2), (3) into (1), solving for ΔP and assuming the velocity error to be $\Delta V = \pm 1$ meter/sec yields:

$$\Delta P = \pm (1.55 \text{ pixels}) \frac{K \cos\theta - 1}{(K - \cos\theta)^2 + \sin^2\theta}, \qquad (4)$$

for an ATS-6 two image sequence with a velocity error of ± 1 m/s.

Equation (4) is used to generate the following table for a two- and three-image sequence. (The image-matching measurements between the first and second and the second and third images in a three-image sequence are assumed to be independent; thus the accuracy in a three-image sequence need only be $1/\sqrt{2}$ times as accurate as for a two-image sequence to obtain wind-speed measurements accurate to 1 m/s.)

Angle	Accuracy in Pixels ΔP Required to Obtain Wind Speed Accuracies Within ± 1 m/s	
	Two-Image Sequence	Three-Image Sequence
θ(degrees)	$\pm \Delta P$ (pixels)	$\pm \sqrt{2}\, \Delta P$ (pixels)
0	.29	.40
10	.28	.39
20	.26	.38
30	.23	.32
40	.18	.26
50	.14	.21
60	.09	.13

TABLE D.1. Accuracy in Pixels Required to Obtain Wind-Speed Accuracies to ± 1 meter per second as a Function of Angle

PPENDIX E. EFFECT OF YAW ANGLE ERRORS ON WIND-MEASUREMENT ACCURACY

The earth-edge shift measurement scheme used to account for relative ttitude changes accounts for roll and pitch changes but cannot account for yaw-angle errors (a yaw-angle change results in an effective rotation of the earth image about the SSP). This appendix derives expressions to estimate the errors on wind-velocity and wind-speed calculations due to yaw angle errors and computes wind-speed errors as a function of angle measured from the SSP line.

For simplicity and without loss of generality, let the earth-centered XYZ coordinate system coincide with the earth-fixed axes relative to which latitude and longitude are measured (Fig. E.1.) and let the satellite be located on the + X axis.

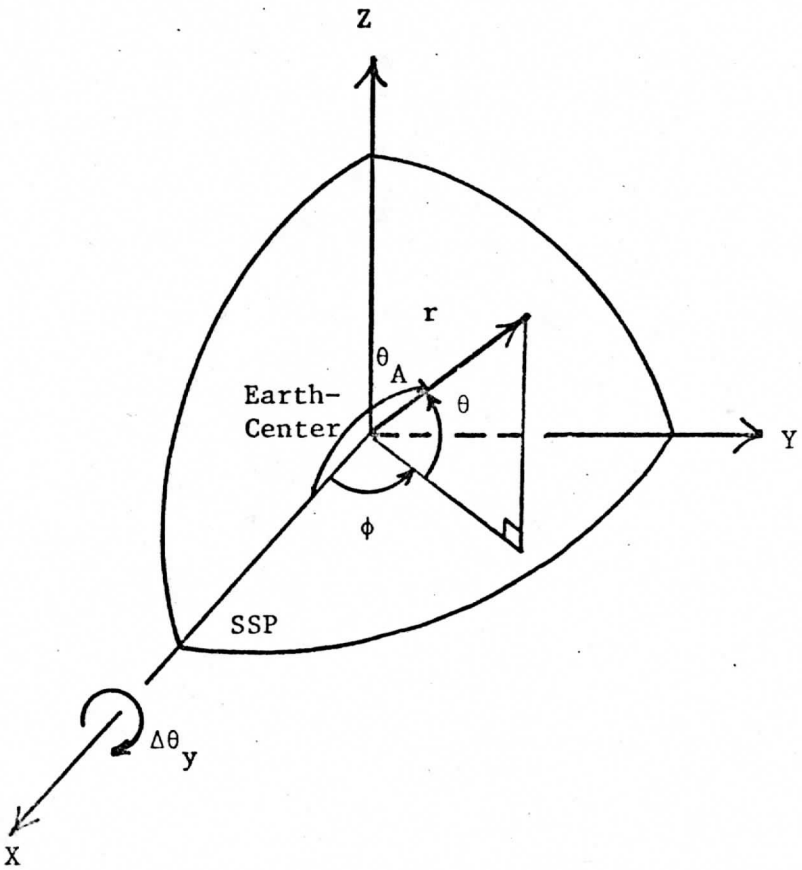

FIGURE E.1. Yaw-Angle Geometry

Define the following:

$\vec{r} = R[X,Y,Z]^T$ = vector locating a point on the earth, radius R, whose scaled components are X, Y, Z. "T" is the transpose of the row vector.

(θ,ϕ) = latitude, longitude corresponding to $\vec{r}$

$\Delta\theta_y$ = yaw-angle change between two successive ATS-6 images separated in time by Δt

$(\Delta U,\Delta V)$ = apparent velocity errors in U- and V-components due to yaw-angle change $\Delta\theta_y$

θ_A = angle between X-axis and $\vec{r}$

ΔV_y = apparent wind-speed error.

The vector $\vec{r}$ expressed in θ and ϕ is

$$\vec{r} = R[X,Y,Z]^T = R[\cos\theta\cos\phi,\ \cos\theta\sin\phi,\ \sin\theta]^T . \qquad (1)$$

Now a yaw-angle change $\Delta\theta_y$ between two consecutive image scans of the point located by $\vec{r}$ (in the first image) over a time Δt results in an effective U- and V-component velocity error given by the expressions:

$$\Delta U = R \frac{\Delta\phi}{\Delta t} \cos\theta \qquad (2)$$

$$\Delta V = R \frac{\Delta\theta}{\Delta t} , \qquad (3)$$

where $\Delta\theta,\Delta\phi$ are the latitude and longitude errors resulting from $\Delta\theta_y$.

The apparent change in $\vec{r},\Delta\vec{r}$ over the time interval Δt due to $\Delta\theta_y$ can be expressed in terms of an infinitesimal rotation by the angle $\Delta\theta_y$ about the X-axis:

$$\Delta\vec{r} = R \begin{bmatrix} 0 & 0 & 0 \\ 0 & 0 & \Delta\theta_y \\ 0 & -\Delta\theta_y & 0 \end{bmatrix} \begin{bmatrix} X \\ Y \\ Z \end{bmatrix}$$

$$= R[0,\ \Delta\theta_y Z,\ -\Delta\theta_y Y]^T$$

$$= R[0,\ \Delta\theta_y \sin\theta,\ -\Delta\theta_y \cos\theta\sin\phi]^T \qquad (4)$$

Now the relationship (1) can be differentiated with respect to θ,ϕ and the differentials replaced by Δ's to yield

$$d\vec{r} \cong \Delta\vec{r}$$

$$\cong R[-\Delta\phi\cos\theta\sin\phi - \Delta\theta\sin\theta\cos\phi,\ \Delta(\cos\theta\sin\phi),\ \Delta\theta\cos\theta]^T \qquad (5)$$

The equality of the X-components in (4) and (5) yields

$$\Delta\phi\cos\theta = -\frac{\Delta\theta\sin\theta\cos\phi}{\sin\phi}\ , \qquad (6)$$

and the equality of the Z-components yields

$$\Delta\theta = -\Delta\theta_y \sin\phi\ . \qquad (7)$$

Substituting (7) into (6) results in

$$\Delta\phi\cos\theta = \Delta\theta_y \sin\theta\cos\phi\ . \qquad (8)$$

Substituting the RHS of (8) into (2) and the RHS of (7) into (3) results in the apparent U- and V-velocity component errors resulting from yaw-angle errors as a function of latitude and longitude:

$$\Delta U = R\frac{\Delta\theta_y}{\Delta t}\sin\theta\cos\phi \qquad (9)$$

$$\Delta V = -R\frac{\Delta\theta_y}{\Delta t}\sin\phi\ . \qquad (10)$$

The total wind-speed error ΔV_y is

$$\Delta V_y = \sqrt{\Delta U^2 + \Delta V^2} = R \frac{\Delta\theta_y}{\Delta t} \sqrt{\sin^2\theta\cos^2\phi + \sin^2\phi}$$

$$= \frac{R\Delta\theta_y}{\Delta t} \sqrt{1 - \cos^2\theta\cos^2\phi} = \frac{R\Delta\theta_y}{\Delta t} \sqrt{1 - \cos^2\theta_A}$$

$$= \frac{R\Delta\theta_y}{\Delta t} \sin\theta_A \ , \qquad (11)$$

where θ_A is the azimuthal angle between the X-axis and $\vec{r}$. ((11) could have been derived directly from very simple geometric considerations, but for the sake of completeness, it was desired to derive the ΔU and ΔV error terms.)

Using the worst-case estimate of $\Delta\theta_y$ as $\pm$ 2.5 pixels, the following can be evaluated:

$$\Delta\theta_y = \frac{\pm\ 2.5 \text{ pixels}}{120 \dfrac{\text{ATS-6 pixels}}{\text{degree}}} \cdot \frac{\pi}{180} \frac{\text{rad}}{\text{deg}} \ ,$$

$$R = 6.378 \times 10^6 \text{ m} \ ,$$

$$\Delta t = 24.6 \text{ min } (60 \text{ sec/min}) \ ,$$

substitution of these values into (11) yields

$$\Delta V_y = 1.57 \sin\theta_A \text{ (m/s)} \ , \qquad (12)$$

for a 2-image ATS-6 sequence, and

$$\Delta V_y = \frac{1.57}{\sqrt{2}} \sin\theta_A = 1.11 \sin\theta_A \text{ (m/s)} \qquad (13)$$

for a 3-image sequence. From (12) and (13) Table E.1 is prepared

Angle θ_A (deg)	Velocity Error ΔV_y due to $\pm$ 2.5 pixel Yaw Error	
	2-image Sequence ($\pm$ m/s)	3-image Sequence ($\pm$ m/s)
0	0	0
10	.27	.19
20	.54	.38
30	.79	.56
40	1.01	.71
50	1.20	.85
60	1.36	.96

TABLE D.1. Velocity Error as a Function of Yaw-Angle Error and Angle

The low-level grid-point interpolated winds measured from ATS-6 images and coinciding with those winds measured from SMS-1 images (TABLE II.2.) span an angular range about the ATS-6 SSP line from 22° to 40°. Thus the largest ATS-6 wind-speed error in a 3-image sequence that could result from a $\pm$ 2.5 pixel yaw-angle error would range from .4 m/s to .7 m/s. As seen from TABLES II.1. and II.2. these values are less than the rms wind-speed errors measured. Thus we can conclude for this image area studied that the effect of yaw-angle error on wind-speed measurements is small compared to other sources of error.

APPENDIX F. EFFECT ON EARTH-EDGE DISPLACEMENT MEASUREMENTS DUE TO ECCENTRICITY OF ATS-6 ORBIT

As discussed in Appendices A and B, the effective attitude changes between successive ATS-6 images as a function of scan line is determined from the measured right and left earth-edge displacements between the successive image scan lines.

Clearly for nonzero eccentricity of the satellite's orbit, the angular size of the earth as seen from the satellite will change from one image to the next.

If this change were large enough, it could affect the attitude-change estimates between consecutive images derived from the earth-edge measurements. This appendix places an upper-bound estimate on the angular change of the earth's image between consecutive ATS-6 images.

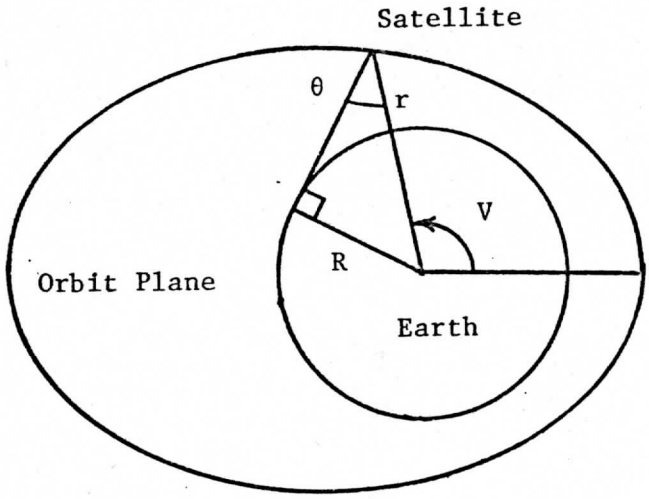

FIGURE F.1. Satellite/Orbit Geometry

Let:

r = distance from the earth-center to the satellite

R = radius of earth

V = true anomaly angle

θ = half-angle that the earth subtends at the satellite

e = eccentricity of ATS-6 satellite's orbit = 2×10^{-4}

$\Delta\theta$ = change in θ over a time interval Δt (for two consecutive ATS-6 images Δt = .41 hours) due to the eccentricity satellite's orbit

a = semi-major axis of orbit $\cong KR$, $K = 6.61$ geosynchronous satellite

The equation of the orbit in terms of r, V and e is:

$$r = \frac{P}{1 + e\cos V}, \quad P = a(1 - e^2) \cong KR(1 - e^2), \tag{1}$$

and since $e \ll 1$, $P \cong KR$ and (1) becomes

$$r \cong KR(1 - e\cos V) . \tag{2}$$

Now the greatest change in r for a change in V occurs when $dr/dV = KRe \sin V$ has its maximum value which occurs when $V = Vm = 90°$; thus

$$(dr/dV)_{max} = KRe . \tag{3}$$

From Fig. F.1., $\sin\theta = R/r$; differentiating both sides and replacing the differentials with Δ's yields:

$$\cos\theta\Delta\theta \cong \frac{R}{r^2}\Delta r \; ; \; \cos\theta \cong \sqrt{1 - \left(\frac{R}{r}\right)^2} = 1,$$

$$\Delta\theta = \frac{R}{r^2}\Delta r \cong \frac{R}{(KR)^2}\Delta r \cong \frac{\Delta r}{K^2 R} \tag{4}$$

The maximum change in $\Delta\theta$ is computed from (4) as follows:

$$\Delta\theta_{max} = \frac{1}{K^2R}\,\Delta r_{max} = \frac{1}{K^2R}\left(\frac{\Delta r}{\Delta V}\right)_{max}\Delta V \qquad (5)$$

$$\cong \frac{KRe}{K^2R}\,\Delta V = \frac{e}{K}\,\Delta V \quad , \qquad (6)$$

where (3) was used to replace $\left(\frac{\Delta r}{\Delta V}\right)_{max}$ with KRe.

Now $\Delta V = (15\ \frac{deg}{hr})(.41\ hr) = 6.15$ deg for an ATS-6 2-image sequence, thus (6) becomes

$$\Delta\theta_{max} = \frac{2 \times 10^{-4}}{6.61}\ 6.15\ \text{deg} = 1.86 \times 10^{-4}\ \text{deg}$$

$$= (1.86 \times 10^{-4}\ \text{deg})(120\ \text{ATS-6 pixels/deg})$$

$$= .02\ \text{ATS-6 pixels.}$$

Thus the worst-case estimate of the eccentricity results in an angular change between successive ATS-6 earth images which is entirely negligible.

APPENDIX G. METHOD OF OBTAINING MIRROR-SCAN-OFFSET CORRECTION CURVES

The nature of the mirror-scan nonlinearity problem has been discussed in previous reports. In order to correct the alternate scan offset caused by this effect, we need a table of offset values as a function of element number (i.e. a $\Delta E(E)$ function). For our initial efforts to produce a $\Delta E(E)$ function, we used the McIDAS cloud-tracking program to measure the displacement of a feature seen in the odd number scans of an image to its position in the even numbered scans of the same image. The method described here is a somewhat more automated scheme and does not require viewing the ATS-6 images. The method has been applied to an IR image (74195 173134Z) and gives good agreement with the old method with less scatter of individual points about a polynomial least-squares fit curve (FIG. G.1.).

In the automated method of computing the $\Delta E(E)$ function a correlation value is computed for the match between a small segment of an odd scan and a shift segment of an adjacent even scan. The amount of shift which gives the best correlation for that small line segment is taken to be the ΔE value for that scan line and element location. Values are computed over many scans and elements, then averaged over the scans. The result is a table of ΔE values as a function of E(element). The table values are then smoothed by using a least squares fit polynomial. In more detail the method is as follows:

Let:

e = element number ($1 \leq e \leq 2400$)

s = scan number ($1 \leq s \leq 1200$)

$p_e(s,e)$ = pixel digital value at a given even-scan, element position

$p_o(s,e)$ = pixel digital value at a given odd-scan, element position

δ = an element shift value

t = a small number defining the length of the scan segment used for a correlation

$C(s,e,\delta)$ = a measure of the match between line segments from adjacent odd and even scans.

Now define C by:

$$C(s,e,\delta) = \sum_{e'=e-t}^{e+t} [p_o(s,e') - p_e(s+1,\ e'+\delta)]^2 \qquad (s \text{ odd})$$

The element shift, ΔE, for a given point on the image (s,e) is the value of δ that gives a minimum value to C:

$$C(s,e,\Delta E(s,e)) \leq C(s,e,\delta) \qquad \forall\delta$$

After an array of these values is generated, a weighted average over scans is taken:

$$\Delta E(e) = \frac{\sum_s w(s,e)\Delta E(s,e)}{\sum_s w(s,e)}$$

The weighting factor is the range of brightness values from the odd scan used in computing C.

$$w(s,e) = MAX(p_o(s,e')) - MIN(p_o(s,e'))$$

where $e - t \leq e' \leq e + t$.

The reason for using this weighting is simply that high contrast features should, in general, produce a correlation value of more significance than features of nearly uniform brightness.

The computer program to do this used the values: $t = 7$ and $+4 \leq \delta \leq 12$. Values of $\Delta E(s,e)$ were computed for every eight scans for the middle third of the image ($s = 399, 407, \ldots, 799$) and for every 10 elements across most of the width of the image ($e = 100, 110, \ldots, 2300$). Using this line and element range some ΔE values will be computed for points off the earth. When off-earth and on-earth points are averaged together the weighting factor will give only a very small or zero weighting to the off-earth points. For some element values no on-earth points are encountered. We found that these points could be determined from the table of $\Delta E(e)$ values. There is a discontinuity between the on-earth and off-earth values.

The $\Delta E(e)$ function is then used to create a corrected image by shifting even scans. An improved method of correcting the alternate scan offset has also been developed. In the old method a fixed shift value was used across the width of a McIDAS image (672 pixels). Although this gave fairly good results, there could be a one or two element alignment error near the edges of the image. The new method, as before, uses the odd scans as a fixed reference. However, the required amount of shift is computed, or looked up in a table, for each pixel in the even scans. Thus the amount of shift varies from one side of the image to the other. Pixels are dropped or doubled, as appropriate, between regions of different shift values.

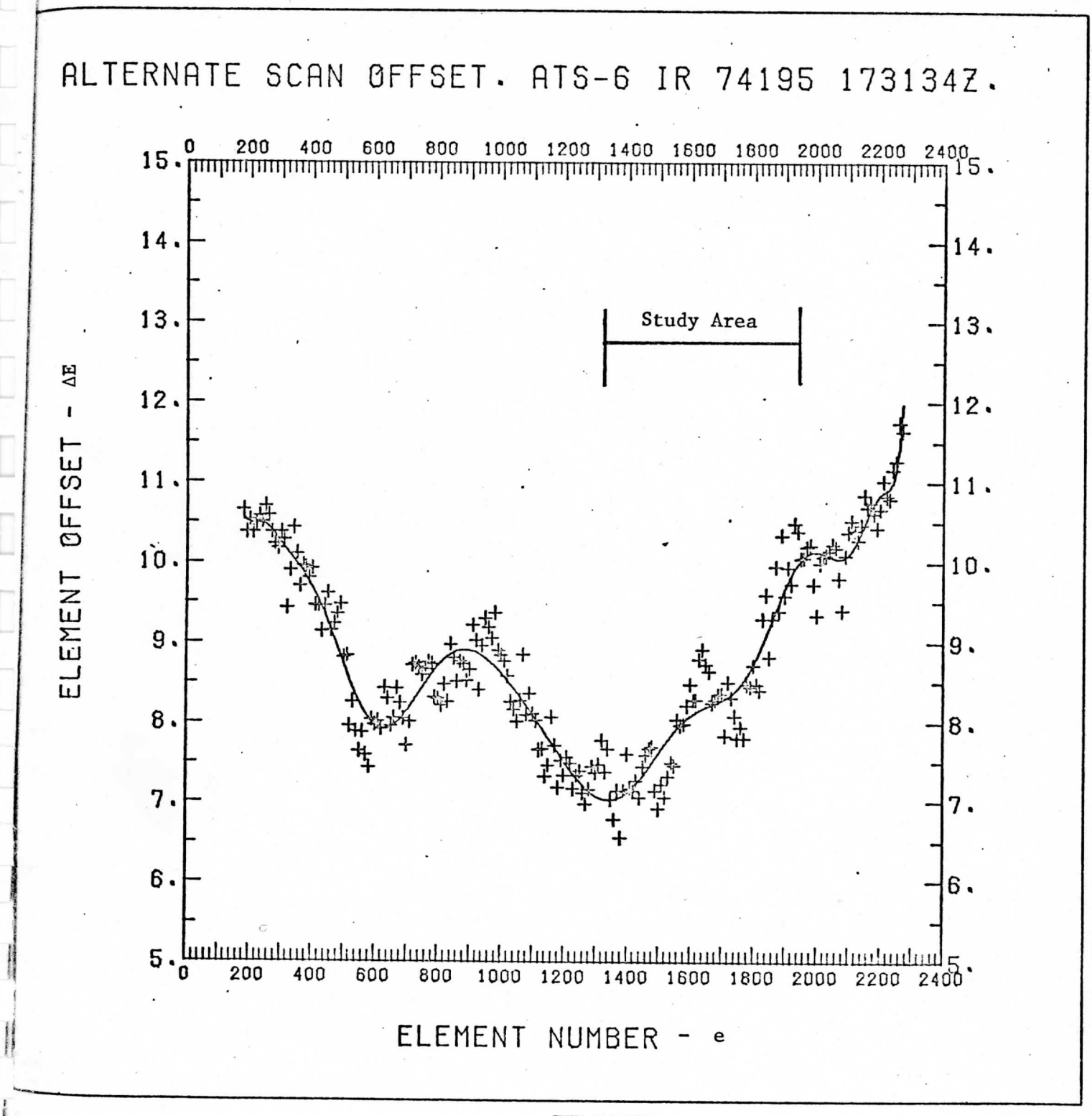

FIGURE G.1. Mirror-Scan Nonlinearity Curve ΔE(e) using newly developed procedure.